An Articulated Closed Kinematic Chain Planar Robotic Leg for High-Speed Locomotion

Yujiong Liu
Robotics and Mechatronics Lab,
Department of Mechanical Engineering,
Virginia Tech,
Blacksburg, VA 24061
e-mail: yjliu@vt.edu

Pinhas Ben-Tzvi[1]
Mem. ASME
Robotics and Mechatronics Lab,
Department of Mechanical Engineering,
Virginia Tech,
Blacksburg, VA 24061
e-mail: bentzvi@vt.edu

This paper presents the design, dynamic modeling, and integration of a single degree of freedom (DOF) robotic leg mechanism intended for tailed quadruped locomotion. The design employs a lightweight six-bar linkage that couples the hip and knee flexion/extension joints mechanically, requiring only a single degree of actuation. By utilizing a parametric optimization, a unique topological arrangement is achieved that results in a foot trajectory that is well suited for dynamic gaits including trot-running, bounding, and galloping. Furthermore, a singular perturbation is introduced to the hybrid dynamic framework to address the lack of robust methods that provide a solution for the differential algebraic equations (DAEs) that characterize closed kinematic chain (CKC) structures as well as the hybrid nature of legged locomotion. By approximating the system dynamics as ordinary differential equations (ODEs) and asymptotically driving the constraint error to zero, CKCs can adopt existing real-time model-based/model-predictive/hybrid-control frameworks. The dynamic model is verified through simulations and the foot trajectory was experimentally validated. Preliminary open-loop planar running demonstrated speeds up to 3.2 m/s. These advantages, accompanied by low-integration costs, warrant this leg as a robust, effective platform for future tailed quadruped research. [DOI: 10.1115/1.4045689]

Keywords: dynamics, legged robots, mechanism design, mobile robots

1 Introduction

Biologically inspired quadrupeds [1–5] and lower extremity rehabilitation engineering [6–10] have primarily focused on leg design and control as the means to ensure dynamic stability during some gaits. However, looking to nature, animals frequently utilize tails to work alongside or in place of their legs to maneuver, stabilize, and/or propel. In conventional quadrupeds, these three functions are all performed by the legs. However, if ground contact cannot be guaranteed—for example, in an unstructured environment with uncertain ground support—the legs' ability to stabilize and maneuver is severely hampered. Integrating a robotic tail with a quadrupedal robot would provide a means of influencing the robot dynamics independent of the ground contact. As a result, the tail could carry the burden of stabilization and maneuvering, leaving the legs primarily responsible for propulsion. Following this idea, a new quadruped locomotion paradigm might be feasible such that each leg's complexity (in terms of degrees of freedom (DOFs)) could be significantly reduced on the account of incorporating a dexterous non-trivial robotic tail [11–13] to replace the stabilizing and maneuvering functions typically provided by highly articulated robotic legs. From the perspective of control, this approach is feasible since the loss of control inputs on legs is compensated by the additional inputs from the tail system. The new paradigm was previously explored and evaluated in hardware-in-the-loop experiments for a reduced complexity quadruped [14] and a reduced complexity biped [15]. Figure 1 illustrates this new locomotion paradigm concept, in which the quadruped subsystem consists of the new leg mechanism discussed in this paper and the R3RT robotic tail subsystem [11]. It is also worth to note that other than the proposed paradigm, the existing approaches to affect the mobile platform without ground contact is to use single link pendulum tails [16–19]. However, for such appendages, limited by their mobility, the locomotion mechanism usually cannot be simplified.

Therefore, this paper aims to develop a reduced DOF planar leg mechanism (1 DOF) that is optimized for high-speed locomotion (specifically for trotting) for tailed planar quadrupeds. The robotic tail subsystem is assumed to help the quadruped achieve stabilization and maneuvering tasks when the robot is airborne. Due to the lack of a complete quadruped prototype at this stage of the research, the leg's performance is evaluated independently on a customized frame that provides structural support for the single leg when performing experiments on a treadmill, which results in a 2D leg dynamics for hopping.

The most commonly used approach to reduce the leg's DOF without violating the foot trajectory is to couple the leg's swing and extension motions by linkages, which yields planar closed kinematic chain (CKC) mechanisms. The articulated nature of legged robots is most effectively captured by a CKC mechanism due to the ability to control passive degrees of freedom with a single

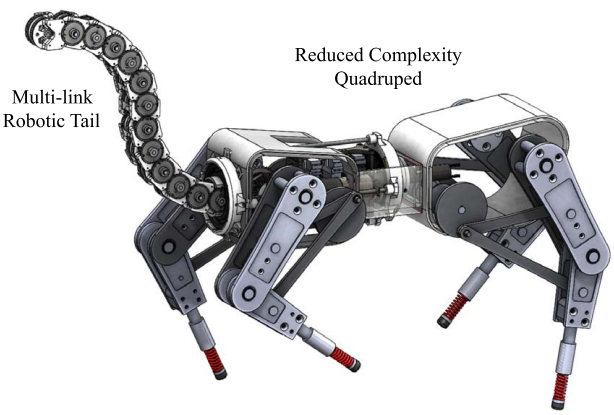

Fig. 1 The concept of using a multi-link robotic tail to maneuver and stabilize a reduced complexity planar quadruped made of four BOLT legs shown in Fig. 2

[1]Corresponding author.

Contributed by the Mechanisms and Robotics Committee of ASME for publication in the Journal of Mechanisms and Robotics. Manuscript received April 27, 2019; final manuscript received December 9, 2019; published online December 12, 2019. Assoc. Editor: Tuhin Das.

actuator through closed chains of linkages. Additional advantages of CKC mechanisms, for the purposes of legged robotics, are reduced weight due to the concentration of actuators at a proximal location and an increased rigidity-to-weight ratio. These properties are of great value in high-speed applications such as dynamic locomotive gaits. While the higher-level control functionalities remain complex due to the hybrid nature of dynamic legged locomotion, an indirect advantage of a single-DOF CKC mechanism is that it mechanically eliminates potential control parameter variations which helps to enhance the robustness of the lower-level trajectory tracking controller; in particular, it directly eliminates the need for the foot trajectory generators and on-board inverse kinematic calculations.

A variety of single-DOF leg mechanisms have been previously implemented and explored [20–23]. A single-DOF walking machine was developed in Ref. [20], while Ref. [21] provided a thorough research on single-DOF leg mechanisms. However, due to their main design purpose being for walking gait, the generated foot trajectories by these designs are all approximately straight lines, which are thought to be unsuitable for fast locomotion (trotting). For fast dynamic locomotion, the ground-contacting time during the stance phase should be minimized, as shown by the sinusoidal wave observations in Ref. [24]. The closest single-DOF to the mechanism in this paper is the cat-inspired leg mechanism which also exhibits fast trotting gait [22]. However, this work relies on the human justification of the leg parameters and thus lacks a concrete theoretical foundation. Therefore, this work advances the mechanism in Ref. [23] through parametric optimization to give a more efficient forward locomotive trotting trajectory.

Besides using linkages to force the motion of the reduced DOF, another way is to simply leave the reduced DOF passive, as shown in the Scout-II robot [25] in which the leg's extension motion is generated by passive springs. However, the prismatic leg design of Scout-II is an oversimplification that results in "robotic-like bounding."

The ramifications of this design choice are revealed during an effort to transform the dynamic model into state-space form. Principally, the CKCs are characterized by algebraic equations (AEs) and the resultant systems of equations that describe the system are identified as differential algebraic equations (DAEs). From a simulation standpoint, numerical solutions of DAEs are more challenging to obtain in comparison with ordinary differential equations (ODEs) [26]. In robotics, constrained mechanisms are defined by index-3 DAEs [27]. The index represents the number of times that holonomic constraints have to be differentiated with respect to time before the form of ODE can be assumed. One of the existing methods in the literature proposes direct interaction with index-3 DAEs through input–output linearization [28]. Another technique suggests differentiation of holonomic constraints twice, thus representing them at the velocity level, and then solving the AE to obtain an implicit state-space representation of the resultant index-1 DAE [29]. However, a by-product of this method is the magnification of drift in the solution. Furthermore, the admissibility of the result is solely dependent on the satisfaction of the initial condition. Drift stabilization formulations have been proposed in the past in Refs. [30,31] to address this issue. Among these, Baumgarte's stabilization method is a widely adopted scheme. Yet, its appeal is shadowed by the difficulty of choosing appropriate parameters to guarantee robustness [32]. Moreover, from the control perspective, as noted in Ref. [33], a rich library of stable model-based controllers exist for dynamics represented by ODEs in explicit state-space form but are not readily extended to DAE descriptions that are implicit in nature. This is a vast topic that exceeds the scope of this paper; therefore, for an in-depth analysis, interested readers are referred to Refs. [34,35].

Beyond conventional practices of dealing with DAEs directly, singular perturbation formulation (SPF) avoids the aforementioned limitations by approximating the DAE as an ODE. They were first implemented on the model of a two-phase flow heat exchanger in Ref. [36] to express the DAEs in explicit state-space form. This method was adapted to a fixed-base CKC robot in Ref. [37] where the AE is substituted by an asymptotically stable ODE that characterizes the constraint violation. The resultant ODE is also known as the fast dynamics ODE [38]. The success of this approach lies in the rapid disappearance of this fast dynamics term, thus resulting in convergence to the slower subsystem as highlighted in Ref. [39]. It is noteworthy that the SPF treatment results in second-order ODEs that are equal in number to the independent generalized coordinates that describe the system. However, the system described in this research is not fixed-base due to the dynamics of legged locomotion; rather it is a floating-base CKC mechanism under hybrid dynamics framework (widely encountered in locomotion dynamics). The lack of established formal methods for approximating ODEs for this scenario motivates the dynamic modeling part in this paper.

The contribution of this paper is two-fold: (1) a single-DOF leg based on CKC mechanism is optimized to generate a unique trotting trajectory specialized for high-speed locomotion of tailed quadrupeds; (2) the extension of SPF to the class of CKC hybrid systems that includes legged robots. These adaptations are adequately generalized for implementation on other floating-base CKC mechanisms.

The remainder of this paper is organized as follows: Sec. 2 details the parametric optimization undertaken on the link lengths to achieve trotting performance, similar to that seen among biological counterparts. The resultant design is described in Sec. 3. Section 4 systematically walks through the formal treatment of SPF on the flight-phase dynamics, which comprise the hybrid framework of dynamic locomotive legs. Numerical analysis of the proposed formulation, utilizing the hybrid dynamic modeling framework, is then developed and the corresponding results are presented in Sec. 5. Section 6 presents the experimental results that reinforce the notion of simplicity the mechanism entails. Finally, Sec. 7 concludes the paper.

2 Bioinspired One-Degree-of-Freedom Leg For Trotting (BOLT)

BOLT, seen in Fig. 2, is the first step toward our efforts in simplifying dynamic legged locomotion while preserving the characteristics of articulated legs. We hypothesize that a reduced-DOF legged mechanism could result in low-integration costs and reduced computational complexity. Furthermore, we anticipate that the role of the reduced number of actuators (DOFs) per leg can be replaced by the addition of a robotic tail [11–13] to balance and maneuver the resultant quadruped. This section details the hardware design of BOLT (Sec. 2.1) and discusses the advantages of kinematic simplification (Sec. 2.2) innate to CKCs.

2.1 Hardware Design. The mechanical design of BOLT is an evolution of the model presented in Ref. [23] as a result of parametric optimization presented in Sec. 3. The leg is roughly the size of an average domestic dog's leg, at 0.53 m in height. It weighs approximately 6.1 kg and is constructed with aerospace-grade AI 6061. It has only one actuated DOF, driven by a brushless direct current (BLDC) motor (MOOG BN34-25EU-02LH) with 355 W rated power, 1350 w peak power (under intermittent operation), that is mounted with a two-stage, 32:1 planetary gearbox and is placed behind the driving link (part i in Fig. 2). An absolute encoder (US Digital MA3-A10-125-B, part vii in Fig. 2) is mounted at a distance and connected to the driving disk via a timing belt to obtain position feedback. An incremental encoder (US Digital E2-5000-315-IE-H-G-3) is mounted for velocity feedback at the back of the motor. Finally, two-stage compliance is provided in the form of a strong die spring (with a stiffness of 65 kN/m) and a rubber pad at the foot to filter the high-frequency components in the impact.

As emphasized, BOLT is a CKC mechanism with two closed loops identified in Figs. 2(*b*) and 2(*c*). Loop 1 is a four-bar mechanism with passive joints at A, B, and D as marked in Fig. 2(*b*). It

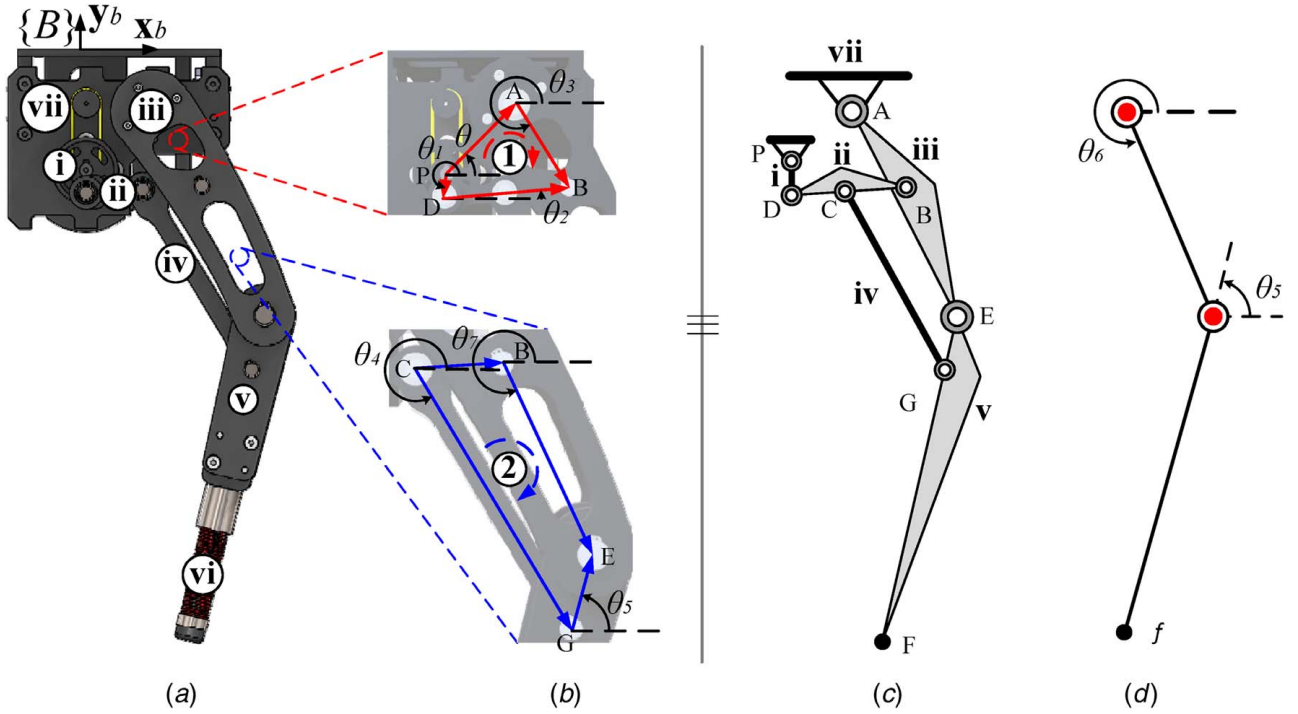

Fig. 2 (*a*) BOLT design and dimension specifications. Left: frontal view: (i) driving disk, (ii) HFE link, (iii) femur, (iv) KFE link, (v) tibia, (vi) double compliance (spring and rubber foot tip), and (vii) absolute encoder; (*b*) close-up view of the two kinematic loops present in the mechanism; (*c*) kinematic diagram of the BOLT mechanism; and (*d*) angular relationships simplify the structure, so that it can be described as an OKC for kinematic purposes

comprises the femur (part iii in Fig. 2) which is guided by the driving disk (part i in Fig. 2) through the help of the hip flexion–extension (HFE) link (part ii in Fig. 2). Loop 2 is another four-bar mechanism that comprises the knee flexion–extension (KFE) link (part iv in Fig. 2) that couples with the motion of the HFE link and guides the tibia (part v in Fig. 2) to execute a smooth continuous trajectory at the foot.

2.2 Kinematic Simplification. This section presents the kinematics of the BOLT mechanism which follows the same procedure as in Ref. [23]. The proposed mechanism eliminates the requirement of multi-actuator coordination, observed in open kinematic chain mechanisms (OKCs), in order to take a single step. The intuitive mechanism couples the hip and knee flexion/extension and thus requires only one actuator for whom, a single revolution corresponds to a single stride. Referring to Figs. 2 and 8, the base link of the six-bar mechanism is fixed at an angle θ. All the other link angles with respect to the x-axis are represented by θ_i, where i denotes the respective body. $i \in \{1, 2 \ldots 5\}$. Note that θ_1 is the crankshaft angle that is known and controlled. In reference to Loop 1 utilizing the kinematic loop closure, the following relation is derived

$$\overrightarrow{PA} + \overrightarrow{AB} - \overrightarrow{PD} - \overrightarrow{DB} = 0 \tag{1}$$

which can be expressed in frame $\{B\}$ using complex numbers, as shown in Eq. (2)

$$l_c e^{i\theta} + l_f e^{i\theta_3} - l_1 e^{i\theta_1} - l_2 e^{i\theta_2} = 0 \tag{2}$$

Further expanding Eq. (2) and utilizing Euler's formula yields the closed-loop constraint equation as

$$\begin{aligned} &l_c \ \cos(\theta) + l_f \ \cos(\theta_3) - l_1 \ \cos(\theta_1) - l_2 \ \cos(\theta_2) \\ &\quad + i(l_c \ \sin(\theta) + l_f \ \sin(\theta_3) - l_1 \ \sin(\theta_1) - l_2 \ \sin(\theta_2)) = 0 \end{aligned} \tag{3}$$

Matlab's *fsolve* function can then be employed to solve for the unknown angles, θ_2 and θ_3. Similarly, the second-loop equations can be formulated to calculate the remaining unknown angles θ_4 and θ_5. Note that θ_7 has a fixed relationship with θ_3, thus can be calculated directly from θ_3. Through kinematic loop closure equations, the system can be represented as an OKC, as seen in Fig. 2(*d*) where θ_6 is the angle of AE with respect to the x-axis. The arrangement of the linkages simplifies the inverse kinematic control problem merely to a one-to-one mapping. The position of the foot, f, is directly linked to the absolute angle of the motor, θ_1. It is then obvious that at any position of the input crank given by the absolute encoder, the position of the foot is known to the system without any significant calculations.

The one-to-one mapping can be implemented in the controller through a lookup table, vastly reducing the computational requirements by removing the need for a foot trajectory generator and the calculation of inverse kinematics.

3 Parametric Optimization of the Mechanism

Conventional legs designed for dynamic locomotion have a 3D workspace, and in certain cases only the 2D workspace, as dictated by the number of actuators provided per leg. This allows for various gaits/maneuvers and on the fly adjustments. However, the single-DOF approach significantly curtails the workspace and restricts the foot to a single traceable trajectory. Therefore, careful design of the mechanism is required in order to achieve the desired performance. This forms the motivation of this section and is addressed through multi-objective parametric optimization.

We intend to integrate this novel six-bar mechanism onto a quadrupedal platform to demonstrate the trot/trot-running gait and as a result, design the desired flight-phase trajectory conducive to this goal in Ref. [23] and pictured in Fig. 3(*b*) for convenience. Additionally, as noted in Ref. [40], the stance trajectory should be sinusoidal. In this paper, the stance phase is defined as the system state that the foot touches the ground (the y-position of the food equals to zero) and the flight phase is defined as the system state that the

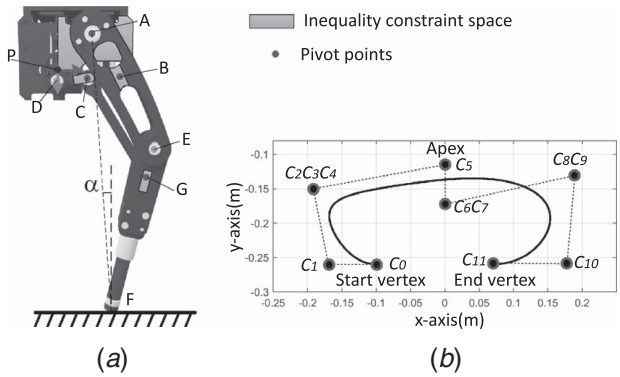

Fig. 3 (*a*) Notation used to formulate the optimization problem, the critical pivots, and their respective constraint evolution space and (*b*) designed ideal trajectory utilized in the optimization

foot does not touch the ground (the y-position of the food is greater than zero).

The combined trajectory is mathematically straightforward and can be abstracted by the desired foot position $f_{des}(\theta_1)$, where θ_1 is the angle made by the crank shaft in body-fixed frame $\{B\}$. Note that the domain of $\theta_1 \in [0 \text{ deg } 360 \text{ deg}]$, and for all computations in this work, counterclockwise is considered positive. The mechanism is illustrated again in Fig. 3(*a*), highlighting the critical pivot locations $A = [A_x\ A_y]$, $B = [B_x\ B_y]$, $C = [C_x\ C_y]$, and $G = [G_x\ G_y]$ that affect the trajectory directly. The leg is parameterized in Fig. 8 and the same convention is followed in this section. The design space is then described by the set $\{\ l_c\ l_1\ l_2\ l_3\ l_4\ l_5\ l_s\ l_f\ l_t\ \theta\}$. An extra parameter of interest is the angle of attack, α, that the leg makes with the vertical line during impact with the ground. The desired trajectory and the minimal angle of attack [41] lead to the formulation of the multi-objective function in Eq. (4), with weights W_1 and W_2

$$obj = W_1\alpha + W_2 \sum_{\theta_1=0^\circ}^{360^\circ} \|f(\theta_1) - f_{des}(\theta_1)\|^2 \tag{4}$$

Here, α is the angle of attack and $f(\theta_1)$ is the current position of the foot with respect to the crankshaft angle θ_1.

3.1 Applied Constraints. In addition to the geometrical constraints defined by the design choices, a set of inequality constraints are prescribed to guide the objective function toward the desired result. The upper and lower bounds are tabulated in Table 1. Equation 5 allows the evolution of the total length of the leg within the provided range

$$l_{leg,lb} \le l_{AE} + l_{EF} \le l_{leg,ub} \tag{5}$$

In order to restrict the pivots A and B to the constraint space highlighted by the meshed regions in Fig. 3(*a*), the objective function is

Table 1 Upper and lower bounds imposed through the inequality constraints on the search space of the link lengths

Parameter	Lower bounds (*lb*) (m)	Upper bounds (*ub*) (m)
l_{leg}	0.45	0.50
l_f	0.073	0.098
l_c	0.075	0.12
l_s	0.039	0.056
l_t	0.044	0.067

Table 2 Optimized design variables

Design variables	Heuristic values	Optimized values
l_c	0.164 m	0.080 m
l_1	0.040 m	0.020 m
l_2	0.180 m	0.105 m
l_3	0.230 m	0.190 m
l_4	0.180 m	0.210 m
l_5	0.290 m	0.303 m
l_s	0.180 m	0.052 m
l_f	0.095 m	0.080 m
l_t	0.062 m	0.050 m
θ	53 deg	41.41 deg

subjected to Eqs. (6) and (7)

$$l_{f,lb} \le \sqrt{(A_x - B_x)^2 + (A_y - B_y)^2} \le l_{f,ub} \tag{6}$$

$$l_{c,lb} \le \sqrt{(A_x - P_x)^2 + (A_y - P_y)^2} \le l_{c,ub} \tag{7}$$

Furthermore, the allowable evolution of pivots, G and C, over the design space is reflected by Eqs. (8) and (9)

$$l_{s,lb} \le \sqrt{(C_x - D_x)^2 + (C_y - D_y)^2} \le l_{s,ub} \tag{8}$$

$$l_{t,lb} \le \sqrt{(G_x - E_x)^2 + (G_y - E_y)^2} \le l_{t,ub} \tag{9}$$

3.2 Optimization Results. With properly formulating the design problem into the optimization framework, existing optimization methods could be used to solve the problem. Due to the vast design space of a six-bar mechanism, the preliminary process of sensitivity analysis is conducted at first (for which the details could be found in Ref. [23]). From the sensitivity analysis, it is found that the crank radius proportionally affects the stride length while the distance between the hip and crank joint inversely affects the angle of attack. With these in mind, a brute-force search is then conducted to find the optimized design parameters.

The optimization resulted in link lengths and angle shown in Table 2 generates a trajectory that closely traces the desired trajectory as shown in Fig. 5(*b*). The angles corresponding to the first loop are depicted in Fig. 4, due to their importance to the knee trajectory. While not pictured, the second-loop angles undergo a similar evolution.

The optimization's validity is proven in the result of the first loop, where the trajectory of the knee is shown to be constrained in the first quadrant, as compared with the trajectory that was the result of heuristic link lengths, as shown in Fig. 5(*a*). The second loop then built upon this outcome, resulting in a sinusoidal stance phase. The flight-phase trajectory in Fig. 5(*b*) can be seen to

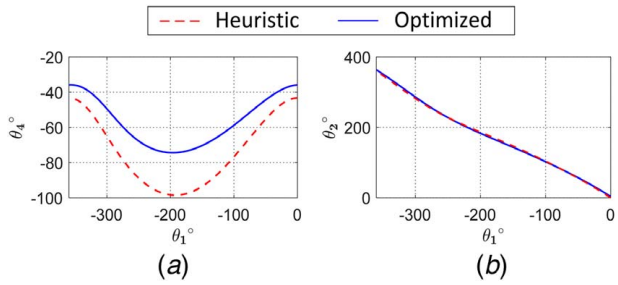

Fig. 4 Comparison of the optimized angular profiles of loop 1 against the profiles obtained from heuristic link lengths in one complete rotation (refer to Ref. [15] for the heuristic foot profile)

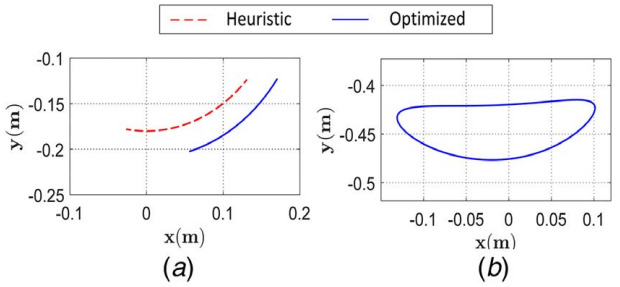

Fig. 5 Comparison of the optimized trajectories of the knee (*a*) and the foot (*b*) against the profiles obtained from heuristic link lengths in one complete rotation. The heuristic foot trajectory is out of scale and not picture here (refer to Ref. [15] for the heuristic foot profile).

possess a slight concavity near the apex, which is attributed to satisfying the multiple inequality constraints posed to the system. All workspace trajectories are measured in the body-fixed frame $\{B\}$.

However, the effect of this concavity on the gait is trivial, as the trajectory still possesses a rapid entrance into the stance phase. The results of the optimization are validated both in simulations and experiments in Secs. 5 and 6, respectively.

4 Dynamic Model of BOLT

This section develops a mathematical description that leverages SPF formulation for imposition onto the hybrid dynamics framework (Sec. 4.1) to alleviate modeling difficulties posed by CKC mechanism, BOLT. It systematically formulates flight-phase dynamics in Sec. 4.2 and stance-phase dynamic in Sec. 4.3 and closes the loop through impact dynamics in Sec. 4.4. Because a complete quadruped prototype is not available, the leg's performance is evaluated independently on a customized framing and a treadmill that constrain the leg's out-of-plane motion and the in-plane pitch rotation. With this experimental setup, the leg's dynamics become a 2D hopper without rotation, i.e., only vertical and horizontally displacements are allowable. Moreover, the passive springs on the foot are ignored (given the selected high stiffness, the passive spring behaves like a rigid body in actual tests) in the dynamic model, which yields a non-elastic impact map in the hybrid dynamics.

The general dynamic equation of motion (EOM) of a system with n links in independent generalized coordinates, denoted by the vector $\mathbf{q} \in \mathbb{R}^{n_q}$ is formulated as

$$\mathbf{H}(\mathbf{q})\ddot{\mathbf{q}} + \mathbf{C}(\mathbf{q}, \dot{\mathbf{q}})\dot{\mathbf{q}} + \mathbf{g}(\mathbf{q}) = \mathbf{B}\boldsymbol{\tau} + \mathbf{F}_{ext} \tag{10}$$

where $\mathbf{H}(\mathbf{q}) \in \mathbb{R}^{n_q \times n_q}$ represents the generalized mass matrix, $\mathbf{C}(\mathbf{q}, \dot{\mathbf{q}}) \in \mathbb{R}^{n_q}$ contains the Coriolis and centrifugal terms, $\mathbf{g}(\mathbf{q})$ is the generalized gravitational force, $\mathbf{B}(\mathbf{q})$ is the actuation Jacobian, and $\boldsymbol{\tau}$ is the torque vector provided by the actuators. The components $\mathbf{F}_{ext}$ will be explored later in this section. Equation (10) results in second-order ODEs identical in dimension to the number of degrees of freedom of the system. Traditional ODE algorithm (for instance, the popular Runge–Kutta methods) can be used to solve this equation easily. However, CKCs like the BOLT mechanism do not benefit from the same properties, as they are identified by high-index DAEs. The implicit nature of DAEs suggests the presence of dependent variables in the dynamic model that describes the mechanism. This coupling of dependent variables with independent variables impedes control design, and hence, such a model is not desired. Most importantly for the development of control algorithms, as highlighted above, it is desired for the model to be defined only by the independent variables. Hence, the EOMs of BOLT warrant prior treatment before they can be expressed in an explicit state-space form. It is worthy to note that the approach in Sec. 2.2 is not applicable for this case since the kinematics in Sec. 2.2 is a numerical solution, which is acceptable for position computation but not for the DAEs from the dynamic modeling. The dynamic equations (ODEs) in the DAEs require velocity and acceleration information which are obtained by differentiating analytic position expressions (forward and inverse kinematics). For CKC, the constraint AEs usually do not yield an analytical solution.

4.1 Hybrid Dynamics Framework. This subsection discusses the term "hybrid dynamic model," which is widely used for modeling locomotion dynamics [42,43], by defining its components in the context of the BOLT. For this hybrid system, a four-tuple $\mathcal{H} = (\mathcal{D}, S, \Delta, \mathcal{F})$ is utilized to describe the complete picture. $\mathcal{D}$ is a set of two domains, where $\mathcal{D}_S$ is the stance domain and $\mathcal{D}_f$ is the flight domain. The stance domain is where the leg is in contact with the ground and the flight domain is where the leg is in the aerial phase. Both domains represent continuous dynamics but differ due to the addition of two coordinates in the flight phase that map the position of the center of mass with respect to the inertial frame, $\{O\}$ as seen in Fig. 8. $S := \{S_S, S_f\}$ is a set of guards that encode the state of the robot at the transition from $\mathcal{D}_S$ to $\mathcal{D}_f$ and vice versa. Note that the constituents of the set S are discrete events which happen instantaneously (i.e., sudden change of state). The continuous and discrete dynamics are tied together by Δ, a set of switching functions. Δ feeds appropriate initializations for the corresponding field, $\mathcal{F}$, of continuous dynamics. A visual representation tailored for BOLTs modes during sagittal running is illustrated in Fig. 6. The mathematical description of each mode follows.

4.2 Underlying Constrained Equation of Motions (Flight-Phase Dynamics). We proceed by first establishing the DAE in this section and the ODE approximation in Sec. 4.3 for the "unpinned system" in flight phase. The method of virtual separation, as in Ref. [44], is adapted to derive the dynamic model of the CKC mechanism under consideration. First, this method prescribes a separation of joints at strategic locations to form serial and branched kinematic chains as highlighted in Fig. 7.

In this work, such a system is denoted as an "unconstrained system." Traditional methods used for serial chains can then be applied to formulate the unconstrained system's EOMs. To capture the dynamic configuration of this floating-base system, two coordinate frames are defined, an inertial reference frame $\{O\}$ and a body-fixed frame $\{B\}$. In the flight phase, two extra coordinates, x_b and y_b, are added to track the position of the body with respect to $\{O\}$. The absolute orientation of the leg in the sagittal plane is notated as q_{Pitch}.

In addition, each link's configuration relative to its previous frame is represented by q_i, with $i = \{1, \ldots, 5\}$. These variables are collected in the vector $\mathbf{q}_d := [q_1\ q_{Pitch}\ x_b\ y_b\ q_2\ q_3\ q_4\ q_5]^T$ and are illustrated in Fig. 8. Furthermore, the masses of the bodies are

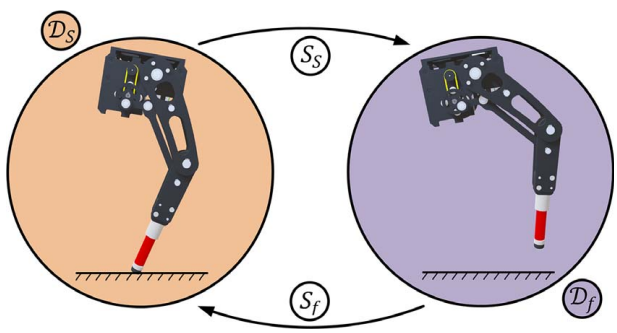

Fig. 6 State machine implementation of the stance and flight phase controller

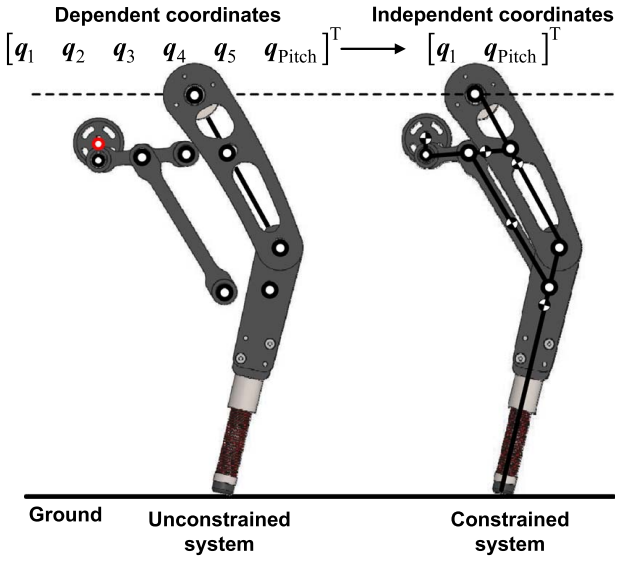

Fig. 7 Illustrating the virtual separation method aided to alleviate modeling of the CKC BOLT robot on the left. Toward the right, rejoining of the separated joints and reduction of generalized coordinates that completely describe the robot is depicted.

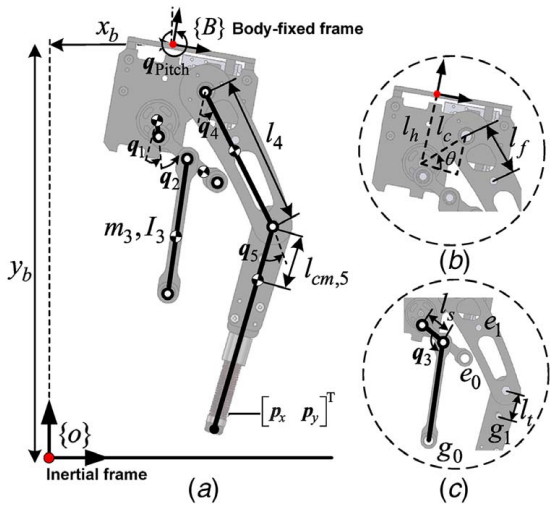

Fig. 8 (*a*) Measurement conventions utilized to derive the dynamic model of BOLT in the flight phase, illustrated as an unconstrained system. (*b*) Relevant link lengths that describe the first closed loop of the system. (c) Depict the constrain definitions employed in the formulation, e0 = e1 and *g*0 = *g*1 and link lengths pertinent to second loop.

given by m_i and the respective inertias by I_i. Similarly, the link lengths are denoted by l_i and the position of the center of mass of each body is given by $l_{cm,i}$. Using Lagrangian formulation, the EOMs of the unconstrained system are then given by

$$\mathbf{H}'(\mathbf{q}_d)\ddot{\mathbf{q}}_d + \mathbf{C}'(\mathbf{q}_d,\ \dot{\mathbf{q}}_d)\dot{\mathbf{q}}_d + \mathbf{g}'(\mathbf{q}_d) = \mathbf{B}\boldsymbol{\tau} + \mathbf{F}_{ext} \tag{11}$$

where $\mathbf{H}'(\mathbf{q}_d) \in \mathbb{R}^{8\times8}$, $\mathbf{C}'(\mathbf{q}_d, \dot{\mathbf{q}}_d) \in \mathbb{R}^{8\times8}$, and $\mathbf{g}'(\mathbf{q}_d) \in \mathbb{R}^8$. From here on, for the sake of brevity, the elements on the right-hand side of the equation, $\boldsymbol{\tau}$ and $\mathbf{F}_{ext}$, are dropped. This term is not affected by the defined process and can be added back later without much effort.

Next, this method dictates the incorporation of constraint equations given by $\boldsymbol{\phi}(\mathbf{q}_d)$ into the mathematical description of the system, thus reconnecting the separated joints and resulting in a constrained system. The corresponding constraint definitions are provided in Fig. 8. The resultant system in the flight phase is characterized by constrained EOMs that are DAEs and assume the form of Eq. (12).

$$\begin{cases} \mathbf{H}'(\mathbf{q}_d)\ddot{\mathbf{q}}_d + \mathbf{C}'(\mathbf{q}_d,\ \dot{\mathbf{q}}_d)\dot{\mathbf{q}}_d + \mathbf{g}'(\mathbf{q}_d) \\ \boldsymbol{\phi}(\mathbf{q}_d) = 0 \end{cases} \tag{12}$$

4.3 Singular Perturbation Formulation Dynamic Formulation. However, as previously stated, the primary goal of this paper is to completely avoid handling the DAEs by approximating them as equivalent ODEs. This section establishes the corresponding mathematical evaluation.

Due to the kinematic coupling present in the mechanism, q_1 alone is sufficient to describe the leg's motion, which in the traditional sense implies that a single ODE is sufficient to characterize the dynamics of the system. Since it is a planar floating-base system, the additional three coordinates x, y, and q_{Pitch} are necessary for a complete description. These four coordinates are therefore termed as independent variables and are included in the vector, $\mathbf{q} := [q_1\ q_{\text{Pitch}}\ x_b\ y_b]^{\mathrm{T}}$. The surplus variables in $\mathbf{q}_d$ are the dependent variables and are included in a separate vector, $\mathbf{z} := [q_2\ q_3\ q_4\ q_5]^{\mathrm{T}}$. To eliminate the first-order derivative terms of $\mathbf{z}$ in Eq. (12) and obtain an explicit description of the CKC leg, the singularly perturbed dynamic model for fixed-base models as in Ref. [37] is leveraged for this floating-base dynamic model.

Given that this minimal order model revolves around the representation of DAEs as ODEs, the problem hinges upon the approximation of the algebraic constraints. Drawing from the work in Ref. [36], we therefore introduce a variable $\mathbf{w} := \boldsymbol{\phi}(\mathbf{q}_d)$ to capture the degree of constraint violation. Ideally, it is desired for this value to asymptotically converge to zero. By definition, $\mathbf{w}$ is an arbitrary variable, allowing the flexibility to decide its dynamic behavior. Hence, we designate $\dot{\mathbf{w}} = -\mathbf{w}/\varepsilon$ to assure the convergence to the invariant set $\{0\}$. Here, ε can accommodate any small positive number. By definition of $\mathbf{w}$, this relationship can then be rewritten as in Eq. (13)

$$\mathbf{J}_z\dot{\mathbf{z}} + \mathbf{J}_q\dot{\mathbf{q}} = -\frac{1}{\varepsilon}\boldsymbol{\phi}(\mathbf{q}_d) \tag{13}$$

where $\mathbf{J}_z$ and $\mathbf{J}_q$ are the corresponding Jacobian matrices. Note that the inclusion of Eq. (13) introduces "fast dynamics" into the model, thus eliminating the algebraic equations. However, the governing ODE in Eq. (12) is still coupled with the second-order terms of the dependent variables in $\mathbf{z}$. Therefore, a dimensionality reduction process is undertaken. To begin, we will consider two selector matrices $\mathbf{S}_q$ and $\mathbf{S}_z$ to encapsulate the relationship that $\mathbf{q}$ and $\mathbf{z}$ hold with $\mathbf{q}_d$. This correlation can be denoted as $\begin{bmatrix}\mathbf{q} & \mathbf{z}\end{bmatrix}^{\mathrm{T}} = \begin{bmatrix}\mathbf{S}_q & \mathbf{S}_z\end{bmatrix}^{\mathrm{T}}\mathbf{q}_d$. Then, $\Gamma(\mathbf{q}_d)$ is formed by combining $\boldsymbol{\phi}(\mathbf{q}_d)$ and $\mathbf{S}_q(\mathbf{q}_d)$ as in Eq. (14)

$$\Gamma(\mathbf{q}_d) = \begin{bmatrix} \boldsymbol{\phi}(\mathbf{q}_d) \\ \mathbf{S}_q(\mathbf{q}_d) \end{bmatrix} \tag{14}$$

Additionally, we can define $\dot{\mathbf{q}}_d = \rho(\mathbf{q}_d)\dot{\mathbf{q}}$, the proof of which is described in Ref. [35]. From this definition, ρ is then given as

$$\rho(\mathbf{q}_d) = \Gamma^{-1}(\mathbf{q}_d)\begin{bmatrix} \mathbf{0}_{4\times4} \\ \mathbf{I}_{4\times4} \end{bmatrix} \tag{15}$$

With this, the dimensionality reduction can then be performed by noting Eq. (15). The reduction can be verified by observing the real coordinate spaces: $\mathbf{H}(\mathbf{q}_d) \in \mathbb{R}^{4\times4}$, $\mathbf{C}(\mathbf{q}_d) \in \mathbb{R}^{4\times4}$, and $\mathbf{g}(\mathbf{q}_d) \in \mathbb{R}^4$. Finally, the model can be pieced together as in Eq. (17), by replacing $\mathbf{q}_d$ with $\mathbf{q}$, $\mathbf{z}$ and combining Eqs. (13) and (16) and the torque terms as in Eq. (10)

$$\begin{cases} \mathbf{H}(\mathbf{q},\ \mathbf{z}) = \rho(\mathbf{q}_d)^{\mathrm{T}}\mathbf{H}'(\mathbf{q}_d) \\ \mathbf{C}(\mathbf{q}_d,\ \dot{\mathbf{q}}_d) = \rho(\mathbf{q}_d)^{\mathrm{T}}\mathbf{C}'(\mathbf{q}_d,\ \dot{\mathbf{q}}_d)\rho(\mathbf{q}_d) + \rho(\mathbf{q}_d)^{\mathrm{T}}\mathbf{H}'(\mathbf{q}_d)\dot{\rho}(\mathbf{q}_d,\ \dot{\mathbf{q}}_d) \\ \mathbf{g}(\mathbf{q}_d) = \rho(\mathbf{q}_d)^{\mathrm{T}}\mathbf{g}'(\mathbf{q}_d) \end{cases} \tag{16}$$

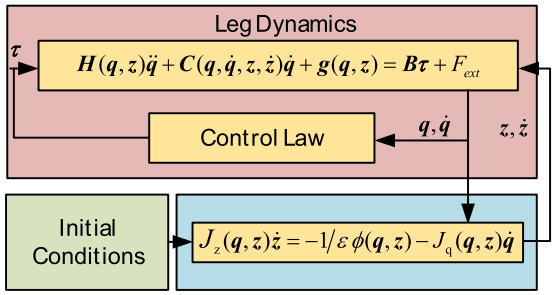

Fig. 9 Illustration of the singularly perturbed dynamic model

$$\begin{bmatrix} \mathbf{H}(\mathbf{q},\mathbf{z}) & \mathbf{0}_{4\times4} \\ \mathbf{0}_{4\times4} & \mathbf{J}_z(\mathbf{q},\mathbf{z}) \end{bmatrix} \begin{bmatrix} \ddot{\mathbf{q}} \\ \dot{\mathbf{z}} \end{bmatrix} = \begin{bmatrix} -\mathbf{C}(\mathbf{q},\dot{\mathbf{q}},\mathbf{z},\dot{\mathbf{z}})\dot{\mathbf{q}} - \mathbf{g}(\mathbf{q},\mathbf{z}) + \mathbf{B}\boldsymbol{\tau} \\ -\dfrac{1}{\varepsilon}\boldsymbol{\phi}(\mathbf{q},\mathbf{z}) - \mathbf{J}_q(\mathbf{q},\mathbf{z})\dot{\mathbf{q}} \end{bmatrix} \tag{17}$$

Equation (17) is the ODE approximation representing the dynamics of the BOLT's flight domain $\mathcal{D}_f$, which is visualized in Fig. 9.

4.4 Impact Model/Reset Map. The impact model is incorporated in the reset map from flight to stance phase and is $\triangle_f^s$. General assumptions are made to arrive at this impact map. This map resets the initial conditions going into the stance phase, hence the name reset map. It assumes that pre-impact states, $(\mathbf{q}_f^-, \dot{\mathbf{q}}_f^-)$, from the flight-phase dynamics are accessible. Post impact states, $(\mathbf{q}_s^+, \dot{\mathbf{q}}_s^+)$, are then provided as an output. Here, the collision is assumed to be instantaneous and is modeled as an inelastic collision. This implies that the position of the feet pre-impact denoted by $\mathbf{q}^-$, and the position of the feet after impact denoted by $\mathbf{q}^+$, are invariable, i.e., $\mathbf{q}^- = \mathbf{q}^+$. Furthermore, an important assumption is that there is no slippage between the feet and ground when contact is made. The impact map, Eq. (18) is obtained by following the approach as detailed in Refs. [42,45], is solved for $\dot{\mathbf{q}}^+$, the generalized velocity after impact

$$\mathbf{H}(\mathbf{q}^+)\dot{\mathbf{q}}^+ - \mathbf{H}(\mathbf{q}^-)\dot{\mathbf{q}}^- = \mathbf{F}_{ext} \tag{18}$$

Likewise, $\dot{\mathbf{q}}^-$ is the velocity prior to impact. Here, the external force, $\mathbf{F}_{ext}$, at the foot end is derived through the principal of virtual work and is projected onto the joint space as

$$\mathbf{F}_{ext} = \mathbf{J}_c^{\mathrm{T}}\mathbf{F} \tag{19}$$

where $\mathbf{J}_c(\mathbf{q},\mathbf{z}) = \partial\mathbf{p}(\mathbf{q},\mathbf{z})/\partial\mathbf{q}$ is the Jacobian of the foot position with respect to $\{O\}$ and $\mathbf{F} = [F_{\mathrm{T}}\ F_{\mathrm{N}}]^{\mathrm{T}}$ is the vector of tangential and normal forces at the foot end.

5 Single-Leg Running Simulation

In the absence of a closed form solution to the dynamics of this hybrid non-linear system, this section validates the SPF hybrid dynamic model of the CKC derived in Sec. 4.3 through numerical simulation. In order to focus the simulation on the verification of the SPF framework and to replicate constraints on the experimental setup, described in Sec. 6.1, BOLT is restricted to the sagittal plane. Furthermore, in this case study, we equate q_{Pitch} to zero and leave it for future work to consider rigorous control treatment for accommodating the pitch angle variance. The model parameters are extracted from the computer-aided design (CAD) model in solidworks and are displayed in Table 3. Simulation details are presented in Sec. 5.1 and its corresponding results are discussed in Sec. 5.2.

Table 3 Mass properties utilized in the simulation

i	Mass (m_i) (kg)	Mass center ($l_{cm,i}$) (m)	Inertia (I_i) (kg m^2)
1	2.5639	0	2.51×10^{-5}
2	0.0802	0.0661	1.53×10^{-4}
3	0.0921	0.1051	4.18×10^{-4}
4	1.1163	0.0574	4.8×10^{-3}
5	0.9754	0.0983	3.9×10^{-3}
6	2.5639	0	2.51×10^{-5}

5.1 Simulation Implementation. The simulation is initialized from the flight phase and is provided with a 14-dimensional initial value vector. The initial conditions include the dependent velocities, abstracted as $\dot{\mathbf{z}}$. However, the output of the SPF hybrid dynamic model then reduces the system to a 10-dimensional output through the decay of the SPF fast dynamics. Upon impact, these outputs are fed to the reset map and the stance-phase initial conditions are calculated. In the stance phase, the fixed frame position and velocity can be extracted using the relationship between the foot and the fixed frame, as the foot is considered a pivot point during this phase.

The flight phase is terminated by a touch-down event when the y-position of the foot decreases to zero. After the touch-down event is detected, the system state is mapped by the impact/reset map into the initial condition for the following stance phase. For the stance phase, once a desired phase angle is reached, a predetermined set point for the angle between the foot and the body-fixed frame at the hip (as seen in Fig. 8), the transition to flight phase is triggered. The stance-phase states are multiplied with the identity matrix encoded within the flight map in order to provide the initial conditions to map back into the flight phase. This cycle is repeated for each step.

It becomes clear that some form of control is necessary in order to a take a single step. Since one focus of this paper is to show the validity of the SPF model, we seek a simple controller. For single-leg running, to move the leg to a desired angle of attack α_m^{des} (through constant speed trajectory tracking) before the next impact is the most basic-level control requirement. The control law is specified in Eq. (20)

$$\tau = K_P(\theta_{1d}(\alpha_m^{des}, t) - \theta_1) - K_D\dot{\theta}_1 \tag{20}$$

Here, θ_{1d} is the desired trajectory of the crankshaft angle, $\dot{\theta}_1$ is the measured angular rate, and K_P and K_D are the proportional and derivative controller gains, respectively. Besides, ±30 N torque limit is applied on the actuator for the flight phase and peak motor power (1350 W, determined based on the motor used in the prototype) constraint is applied for the stance phase. The angle of attack is set to 0 deg.

5.2 Simulation Results. The simulation was performed for 16 steps (around 1.3 m/s), and frames of the simulation running are shown in Fig. 10. The simulation demonstrated the SPF model was successful in the hybrid framework, as shown by the constraints holding throughout the simulation. The constraint errors were abstracted by $w_1 - w_4$, where w_1 and w_2 correspond to the x and y errors of the constraint equation generated by the condition $e_0 = e_1$ (defined in Fig. 8(*c*)), while w_3 and w_4 represent the x and y errors for the condition $g_0 = g_1$ (defined in Fig. 8(*c*)).

As seen in Fig. 11, constraint errors asymptotically track to zero and maintain this behavior during state transitions. In the figure, the squares highlight the transition from stance to stride phase and vice versa, while the rectangular block denotes stance phase.

Figures 12(*a*) and 12(*b*) shows the x and y position of the body-fixed frame with respect to the inertial frame over time. This demonstrates that the simulation successfully obtained single-leg running, with a monotonically increasing x-position and a cyclical y-position. The periodicity in y and q_1 are shown in Fig. 12(*c*)

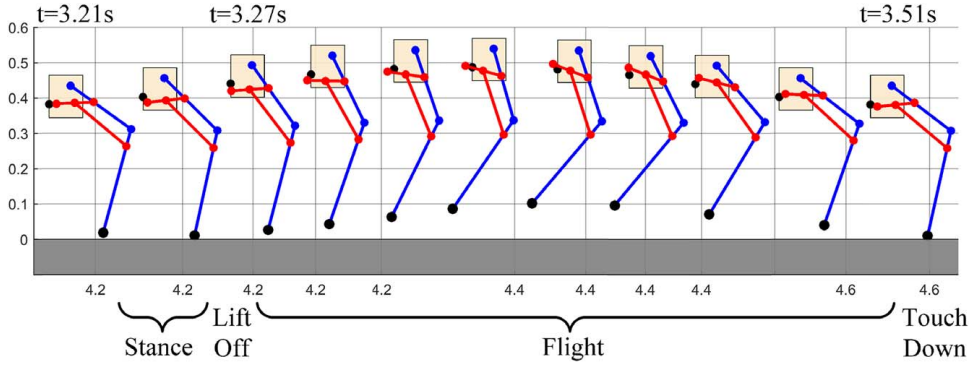

Fig. 10 Sample frames of the BOLT simulated running with a 0.03 s time interval. Note that since the figure is made by combining multiple frames, the ticks on the *x* axis are not linear. Each frame only refers to the tick with the same order (for instance, the fifth frame refers to the fifth tick for positioning).

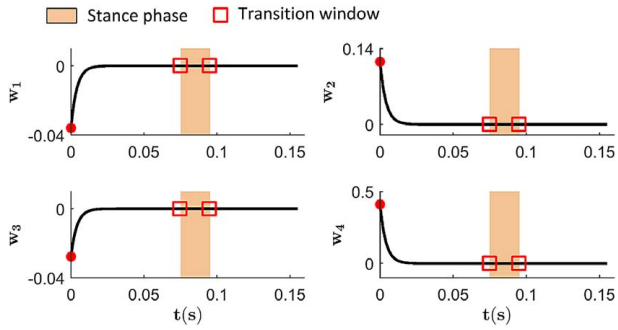

Fig. 11 The constraint errors asymptotically track to zero and constraints are invariant to the hybrid dynamic framework

and 12(*d*) through the limit cycle. In Fig. 12(*c*), the vertical straight line indicates the instantaneous impact while in Fig. 12(*d*), the impact happens on the slanting line, which is due to the coincidence of the full rotation and the impact (i.e., the impact happens when q_1 reaches 360 deg which is also 0 deg). The commanded angle of q_1 is shown in Fig. 13 and the results of the dependent angles are found in Fig. 14. The ranges shown by these angles correspond to the ranges obtained in the optimization, relative to the motion of q_1. Note that the vertical lines in Fig. 13 indicate full rotations (360 deg = 0 deg).

6 Experimental Results

This section describes the integration and evaluation of a prototype BOLT. Foot trajectory obtained as a result of parametric optimization in Sec. 3.2 is validated. Additionally, preliminary open-loop planar running experiment is performed to demonstrate the robot's inherent lower-level control simplicity and achievable speeds under ideal conditions.

6.1 Experimental Setup. Since BOLT is a planar mechanism, its mobility is constrained to the sagittal plane using a custom framing, as shown in Fig. 15(*a*). The framing is mounted onto a commercially available treadmill to evaluate the running performance of the robot. The motor is commanded by the low-level controller via a Teensy microcontroller, while a higher-level controller

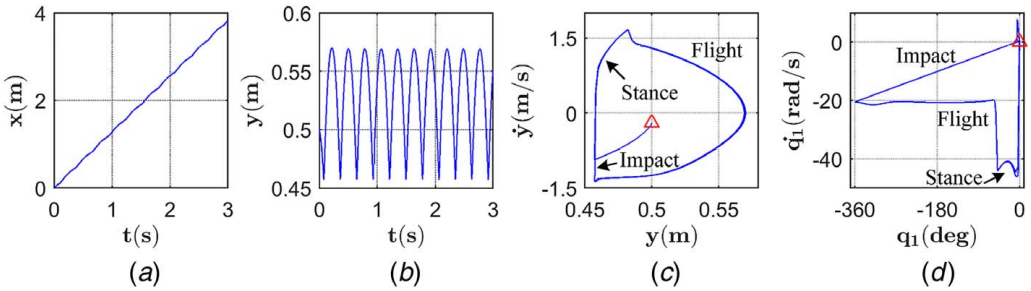

Fig. 12 BOLT running simulation results: (*a*) horizontal position, (*b*) vertical position, (*c*) phase portrait of the height showing limit cycles, and (*d*) phase portrait of the crank angle (q_1) showing limit cycles

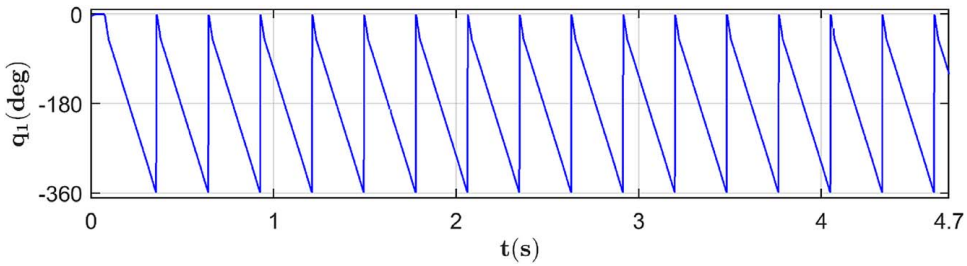

Fig. 13 Commanded angle of the driving joint (q_1) over time

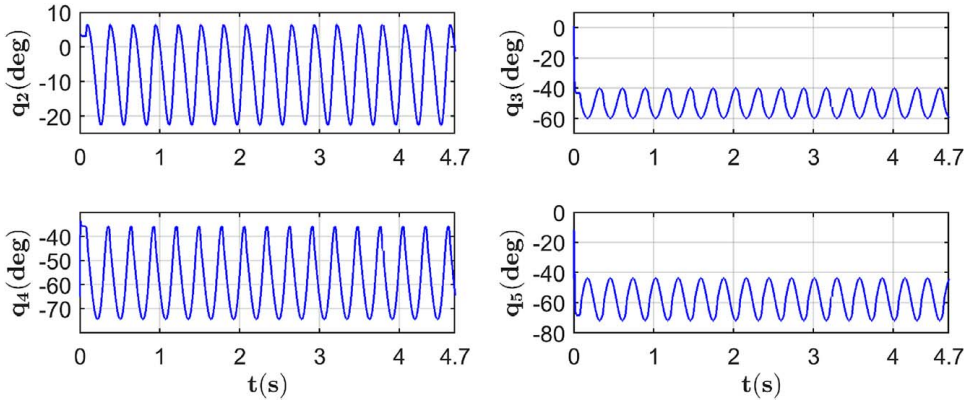

Fig. 14 Angular behavior of the dependent variables (z) over time

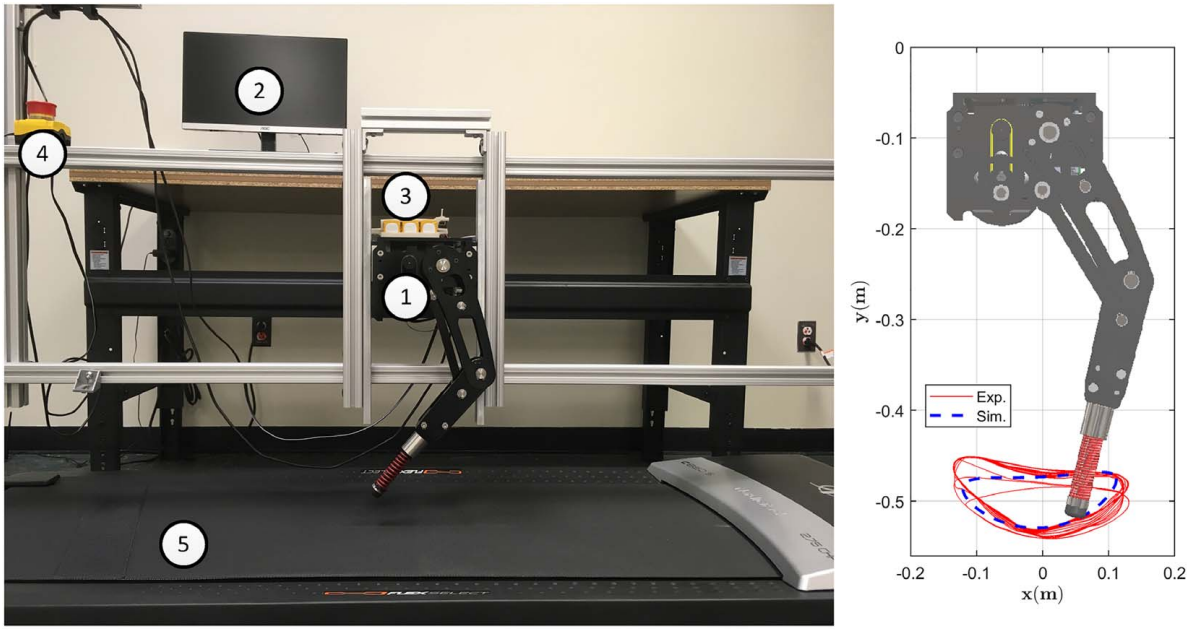

Fig. 15 (*a*) Setup for testing BOLTs running gait: (1) BOLT, (2) higher-level controller, (3) LiPo batteries in series, (4) emergency stop, and (5) treadmill. (*b*) Illustration of trajectory tracking experimental results (in thin solid line) where the thick dashed line is the theoretical foot trajectory.

runs on a computer and provides the Teensy with speed commands. Three 14.8 V LiPo batteries are connected in series (32.56 Whrs) to power the robot.

The first experiment was focused on trajectory validation, where the leg was raised above the treadmill surface and constrained in both the x and y directions. A visual object tracking system, LOSA [46], was attached to the rubber pad of the foot and its trajectory was recorded.

The second experiment demonstrated open-loop running, wherein the leg was unconstrained in the x and y directions. A minimum y position was imposed with a bumper to protect the hardware. BOLT was experimented at multiple speeds from 0.5 m/s to a maximum of 3.2 m/s to observe consistency of performance, with the treadmill speed matched in order to achieve in-place running.

6.2 Experimental Results. To validate the results of the topological optimization (Sec. 3.1), a trajectory tracking experiment was performed. Leveraging the millimeter accuracy of the LOSA object tracking system, the foot trajectory was recorded and is shown in Fig. 15(*b*). The experiments reveal the success of the optimization,

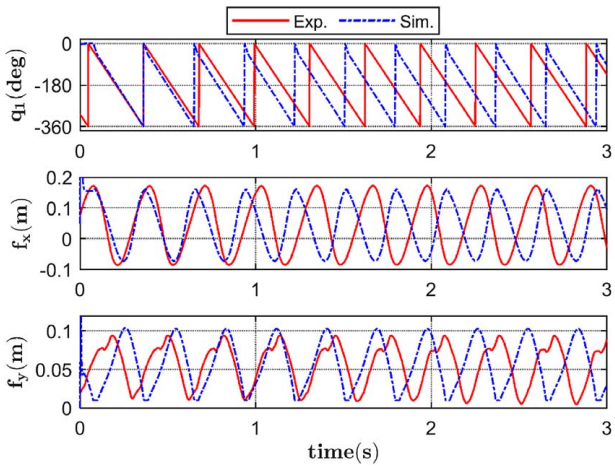

Fig. 16 Comparisons between the simulated results and the experimental data. The bottom two subfigures are the foot position measured in the global frame.

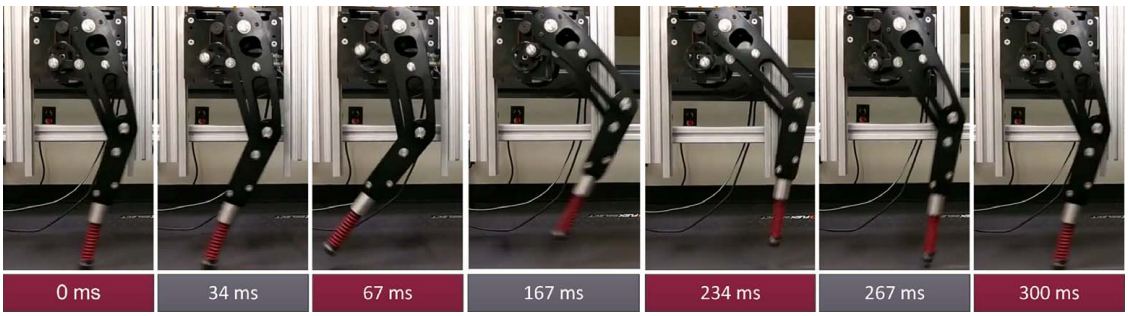

Fig. 17 Sequence of snapshots showing BOLT's running cycle at 3.2 m/s measured on the treadmill

as the stride length and height correspond to those resulting from the kinematic simulations performed following the optimization. As evident from Fig. 15(*b*), the foot tracked a trajectory close to the designed trajectory. The small inconsistencies in the trajectory are due to vibration in the framing due to high speeds.

Performance comparison between the simulated results and the experimental data is shown in Fig. 16. The experimental data is shifted to synchronize with the simulation for the first stride. Since the simulated leg runs on the ground (running forward in the global frame) while the actual leg runs in the air (raised above the treadmill surface), direct comparison of the foot positions is not possible. Therefore, the simulated foot position x component (f_x) is recalculated back to its local frame $\{B\}$ while the y component (f_y) remains unchanged. Figure 16 shows that the experiment exhibits similar behavior as in the simulation. However, the simulation exhibits a faster running motion than the experiment. In fact, the stride time is 284 ms for the simulation and around 315 ms for the experiment.

Due to the lack of the closed-loop controller, direct comparison between the simulated running and the experimental running is not achievable at present. Open-loop running can be seen in the sequence shown in Fig. 17. The sequence depicts a single stride cycle at 3.2 m/s. Note that the speed is measured by reading the treadmill speed when the robot achieves stable running. The actual ground running speed will be lower than the treadmill measured speed (because running on treadmill requires less energy). The open-loop running shows the promise of the mechanism in performing quadrupedal gaits on a flat terrain, as well as its capability to achieve the targeted speed.

7 Conclusion

In this paper, we introduced BOLT, a novel planar CKC mechanism that was designed to execute dynamic locomotive gaits for tailed quadruped robots. The results of parametric optimization were presented, and the SPF hybrid dynamic framework was introduced to reduce the computational cost of CKC modeling such that the model can be utilized to build model-based controllers on high-speed real-time systems. In simulation, the validity of the constraints proposed by the SPF model was confirmed, further demonstrating the model's value for implementation on real-time controllers. Experimentally, the optimization results of BOLT were shown to validate the designed trajectory and successful open-loop running was performed, illustrating the simplicity and its potential to perform dynamic gaits when integrated as a quadruped.

Future work will mainly focus on developing and implementing the model-based feedback controller for running. After the leg is properly controlled, a quadruped with multi-link tail prototype will be built and tested to verify the tailed reduced complexity quadruped idea.

Acknowledgment

The authors would like to acknowledge Mr. Vinay Kamidi's contributions to the original draft of this manuscript. This research is based upon work supported by the National Science Foundation under Grant No. 1906727.

Appendix A

Referring to Fig. 8, the equation of motion during the flight-phase in dependent generalized coordinates is given by Eq. (A1). Since q_{Pitch} is restricted by the custom framing, the dimension of the equation of motion is reduced to 7

$$\begin{cases} \mathbf{H}'(\mathbf{q}_d)\ddot{\mathbf{q}}_d + \mathbf{C}'(\mathbf{q}_d, \dot{\mathbf{q}}_d)\dot{\mathbf{q}}_d + \mathbf{g}'(\mathbf{q}_d) \\ \boldsymbol{\phi}(\mathbf{q}_d) = 0 \end{cases} \tag{A1}$$

Matrix $\mathbf{H}'$ terms are listed as follows. Due to the symmetry of the inertia matrix, only the upper triangle terms of $\mathbf{H}'$ are provided. All unlisted terms are zero

$$\mathbf{H}_{1,1}(\mathbf{q}_d) = I_1 + I_2 + I_3 + l_1^2 m_2 + l_{cm,2}^2 m_2 + l_{cm,3}^2 m_3 + l_s^2 m_3 + 2l_1 l_{cm,3} m_3 \cos(q_2 + q_3) + 2l_1 l_{cm,2} m_2 \cos(q_2) + 2l_1 l_s m_3 \cos(q_2) + 2l_{cm,3} l_s m_3 \cos(q_3)$$

$$\mathbf{H}_{1,2}(\mathbf{q}_d) = -0.5(m_3(2l_s \sin(q_1 + q_2) + 2l_1 \sin(q_1) + 2l_{cm,3} \sin(q_1 + q_2 + q_3))) - 0.5(m_2(2l_{cm,2} \sin(q_1 + q_2) + 2l_1 \sin(q_1)))$$

$$\mathbf{H}_{1,3}(\mathbf{q}_d) = -0.5(m_3(2l_s \cos(q_1 + q_2) + 2l_1 \cos(q_1) + 2l_{cm,3} \cos(q_1 + q_2 + q_3))) + 0.5(m_2(2l_{cm,2} \cos(q_1 + q_2) + 2l_1 \cos(q_1)))$$

$$\mathbf{H}_{1,4}(\mathbf{q}_d) = I_2 + I_3 + l_{cm,2}^2 m_2 + l_{cm,3}^2 m_3 + l_s^2 m_3 + l_1 l_{cm,3} m_3 + \cos(q_2 + q_3) + l_1 l_{cm,2} m_2 \cos(q_2) + l_1 l_s m_3 \cos(q_2) + 2l_{cm,3} l_s m_3 \cos(q_3)$$

$$\mathbf{H}_{1,5}(\mathbf{q}_d) = I_3 + l_{cm,3}^2 m_3 + l_1 l_{cm,3} m_3 \ \cos(q_2 + q_3) + l_{cm,3} l_s m_3 \ \cos(q_3)$$

$$\mathbf{H}_{2,2}(\mathbf{q}_d) = m_1 + m_2 + m_3 + m_4 + m_5 + m_b$$

$$\mathbf{H}_{2,4}(\mathbf{q}_d) = -0.5(m_3(2l_s \ \sin(q_1 + q_2) + 2l_{cm,3} \sin(q_1 + q_2 + q_3))) - l_{cm,2} m_2 \ \sin(q_1 + q_2)$$

$$\mathbf{H}_{2,5}(\mathbf{q}_d) = -l_{cm,3} m_3 \ \sin(q_1 + q_2 + q_3)$$

$$\mathbf{H}_{2,6}(\mathbf{q}_d) = -0.5(m_5(2l_{cm,5} \sin(q_4 + q_5) + 2l_4 \sin(q_4))) - l_{cm,4} m_4 \ \sin(q_4)$$

$$\mathbf{H}_{2,7}(\mathbf{q}_d) = -l_{cm,5} m_5 \ \sin(q_4 + q_5)$$

$$\mathbf{H}_{3,3}(\mathbf{q}_d) = m_1 + m_2 + m_3 + m_4 + m_5$$

$$\mathbf{H}_{3,4}(\mathbf{q}_d) = 0.5(m_3(2l_s \ \cos(q_1 + q_2) + 2l_{cm,3} \ \cos(q_1 + q_2 + q_3))) + l_{cm,2} \mathrm{m}_2 \ \cos(q_1 + q_2)$$

$$\mathbf{H}_{3,5}(\mathbf{q}_d) = l_{cm,3} m_3 \ \cos(q_1 + q_2 + q_3) + \ l_1 l_{cm,2} m_2 \ \cos(q_2)$$

$$\mathbf{H}_{3,6}(\mathbf{q}_d) = 0.5(m_5(2l_{cm,5} \ \cos(q_4 + q_5) + 2l_4 \ \cos(q_4))) + l_{cm,4} \mathrm{m}_4 \ \cos(q_4)$$

$$\mathbf{H}_{3,7}(\mathbf{q}_d) = l_{cm,5} m_5 \ \cos(q_4 + q_5)$$

$$\mathbf{H}_{4,4}(\mathbf{q}_d) = I_2 + I_3 + l_{cm,2}^2 m_2 + l_{cm,3}^2 m_3 + l_s^2 m_3 + 2l_{cm,3} l_s m_3 \ \cos(q_3)$$

$$\mathbf{H}_{4,5}(\mathbf{q}_d) = I_3 + l_{cm,3}^2 m_3 + l_{cm,3} l_s m_3 \ \cos(q_3)$$

$$\mathbf{H}_{5,5}(\mathbf{q}_d) = I_3 + l_{cm,3}^2 m_3$$

$$\mathbf{H}_{6,6}(\mathbf{q}_d) = I_4 + I_5 + l_4^2 m_5 + l_{cm,4}^2 m_4 + l_{cm,5}^2 m_5 + 2l_4 l_{cm,5} m_5 \ \cos(q_5)$$

$$\mathbf{H}_{6,7}(\mathbf{q}_d) = I_5 + l_{cm,5}^2 m_5 + l_4 l_{cm,5} m_5 \ \cos(q_5)$$

$$\mathbf{H}_{7,7}(\mathbf{q}_d) = I_5 + l_{cm,5}^2 m_5$$

Matrix $\mathbf{C}'$ terms are listed as follows. The unlisted terms are all zero

$$\mathbf{C}_{1,1}(\mathbf{q}_d) = -\dot{q}_3(l_1 l_{cm,3} m_3 \ \sin(q_2 + q_3) + l_{cm,3} l_s m_3 \ \sin(q_3)) - \dot{q}_2(l_1 l_{cm,3} m_3 \ \sin(q_2 + q_3) + l_1 l_{cm,2} m_2 \ \sin(q_2) + l_1 l_s m_3 \sin(q_2))$$

$$\begin{aligned}\mathbf{C}_{1,4}(\mathbf{q}_d) = &-\dot{q}_3(l_1 l_{cm,3} m_3 \ \sin(q_2 + q_3) + l_{cm,3} l_s m_3 \ \sin(q_3)) - \dot{q}_1(l_1 l_{cm,3} m_3 \ \sin(q_2 + q_3) + l_1 l_{cm,2} m_2 \ \sin(q_2) \\ &+ l_1 l_s m_3 \ \sin(q_2)) - \dot{q}_2(l_1 l_{cm,3} m_3 \ \sin(q_2 + q_3) + l_1 l_{cm,2} m_2 \ \sin(q_2) + l_1 l_s m_3 \sin(q_2))\end{aligned}$$

$$\mathbf{C}_{1,5}(\mathbf{q}_d) = -(\dot{q}_1 + \dot{q}_2 + \dot{q}_3)(l_1 l_{cm,3} \, m_3 \ \sin(q_2 + q_3) + l_{cm,3} \, l_s m_3 \ \sin(q_3))$$

$$\begin{aligned}\mathbf{C}_{2,1}(\mathbf{q}_d) = &-\dot{q}_1(0.5(m_3(2l_s \ \cos(q_1 + q_2) + 2l_1 \ \cos(q_1) + 2l_{cm,3} \ \cos(q_1 + q_2 + q_3))) + 0.5(m_2(2l_{cm,2} \ \cos(q_1 + q_2) + 2l_s \ \cos(q_1)))) \\ &- \dot{q}_2(0.5(m_3(2l_s \ \cos(q_1 + q_2) + 2l_{cm,3} \ \cos(q_1 + q_2 + q_3))) + l_{cm,2} m_2 \ \cos(q_1 + q_2)) - \dot{q}_3 l_{cm,3} m_3 \ \cos(q_1 + q_2 + q_3)\end{aligned}$$

$$\begin{aligned}\mathbf{C}_{2,4}(\mathbf{q}_d) = &-\dot{q}_1(0.5(m_3(2l_s \ \cos(q_1 + q_2) + 2l_{cm,3} \ \cos(q_1 + q_2 + q_3))) \ + l_{cm,2} m_2 \ \cos(q_1 + q_2)) \\ &- \dot{q}_2(0.5(m_3(2l_s \ \cos(q_1 + q_2) + 2l_{cm,3} \ \cos(q_1 + q_2 + q_3))) + l_{cm,2} m_2 \ \cos(q_1 + q_2)) \\ &- \dot{q}_3 l_{cm,3} m_3 \ \cos(q_1 + q_2 + q_3)\end{aligned}$$

$$\mathbf{C}_{2,5}(\mathbf{q}_d) = -\dot{q}_1 l_{cm,3} \, m_3 \ \cos(q_1 + q_2 + q_3) - \dot{q}_2 \, l_{cm,3} m_3 \ \cos(q_1 + q_2 + q_3) - \dot{q}_3 l_{cm,3} m_3 \ \cos(q_1 + q_2 + q_3)$$

$$\mathbf{C}_{2,6}(\mathbf{q}_d) = -\dot{q}_4(0.5(m_5(2l_{cm,5} \ \cos(q_4 + q_5) + 2l_4 \ \cos(q_4))) + l_{cm,4} \, m_4 \ \cos(q_4)) - \dot{q}_5 l_{cm,5} \, m_5 \ \cos(q_4 + q_5)$$

$$\mathbf{C}_{2,7}(\mathbf{q}_d) = -\dot{q}_4 l_{cm,5} m_5 \ \cos(q_4 + q_5) - \dot{q}_5 l_{cm,5} m_5 \ \cos(q_4 + q_5)$$

$$\mathbf{C}_{3,1}(\mathbf{q}_d) = -\dot{q}_1(0.5(m_3(2l_s\ \sin(q_1+q_2)+2l_1\ \sin(q_1)+2l_{cm,3}\sin(q_1+q_2+q_3))))+0.5(m_2(2l_{cm,2}\sin(q_1+q_2)+2l_1\ \sin(q_1))))$$
$$-\dot{q}_2(0.5(m_3(2l_s\ \sin(q_1+q_2)+2l_{cm,3}\sin(q_1+q_2+q_3)))\ +\ l_{cm,2}m_2\ \sin(q_1+q_2))-\ \dot{q}_3l_{cm,3}m_3\sin(q_1+q_2+q_3)$$

$$\mathbf{C}_{3,4}(\mathbf{q}_d) = -\dot{q}_1(0.5(m_3(2l_s\ \sin(q_1+q_2)+2l_{cm,3}\ \sin(q_1+q_2+q_3)))\ +l_{cm,2}m_2\ \sin(q_1+q_2)-\dot{q}_2(0.5(m_3 2l_s\ \sin(q_1+q_2)$$
$$+2l_{cm,3}\sin(q_1+q_2+q_3)))+l_{cm,2}m_2\ \sin(q_1+q_2))-\ \dot{q}_3l_{cm,3}m_3\ \sin(q_1+q_2+q_3)$$

$$\mathbf{C}_{3,5}(\mathbf{q}_d) = -\dot{q}_1l_{cm,3}m_3\ \sin(q_1+q_2+q_3)-\dot{q}_2l_{cm,3}m_3\ \sin(q_1+q_2+q_3)-\dot{q}_3l_{cm,3}m_3\sin(q_1+q_2+q_3)$$

$$\mathbf{C}_{3,6}(\mathbf{q}_d) = -\dot{q}_4(0.5(m_5(2l_{cm,5}\sin(q_4+q_5)+2l_4\ \sin(q_4)))+l_{cm,4}\ m_4\ \sin(q_4))-\dot{q}_5l_{cm,5}m_5\ \sin(q_4+q_5)$$

$$\mathbf{C}_{3,7}(\mathbf{q}_d) = -\dot{q}_4l_{cm,5}m_5\ \sin(q_4+q_5)-\dot{q}_5l_{cm,5}m_5\ \sin(q_4+q_5)$$

$$\mathbf{C}_{4,1}(\mathbf{q}_d) = \dot{q}_1(l_1l_{cm,3}m_3\ \sin(q_2+q_3)+l_1l_{cm,2}m_2\ \sin(q_2)+l_1l_sm_3\ \sin(q_2)-\dot{q}_3l_{cm,3}l_sm_3\ \sin(q_3)$$

$$\mathbf{C}_{4,4}(\mathbf{q}_d) = -\dot{q}_3l_{cm,3}l_sm_3\ \sin(q_3)$$

$$\mathbf{C}_{4,5}(\mathbf{q}_d) = -\ \dot{q}_1l_{cm,3}l_sm_3\ \sin(q_3)-\dot{q}_2l_{cm,3}l_sm_3\ \sin(q_3)-\dot{q}_3l_{cm,3}l_sm_3\ \sin(q_3)$$

$$\mathbf{C}_{5,1}(\mathbf{q}_d) = \dot{q}_1(l_1l_{cm,3}m_3\ \sin(q_2+q_3)+l_{cm,3}l_sm_3\ \sin(q_3))+\ \dot{q}_2l_{cm,3}l_sm_3\ \sin(q_3)$$

$$\mathbf{C}_{5,4}(\mathbf{q}_d) = \dot{q}_1l_{cm,3}l_sm_3\ \sin(q_3)+\dot{q}_2l_{cm,3}l_s\ m_3\ \sin(q_3)$$

$$\mathbf{C}_{6,6}(\mathbf{q}_d) = -\dot{q}_5l_4l_{cm,5}m_5\ \sin(q_5)$$

$$\mathbf{C}_{6,7}(\mathbf{q}_d) = -\dot{q}_4l_4l_{cm,5}m_5\ \sin(q_5)-\dot{q}_5l_4l_{cm,5}m_5\ \sin(q_5)$$

$$\mathbf{C}_{7,6}(\mathbf{q}_d) = \dot{q}_4l_4l_{cm,5}m_5\ \sin(q_5)$$

Vector $\mathbf{g}'$ terms are listed as follows:

$$\mathbf{g}_1(\mathbf{q}_d) = gm_3(l_s\ \cos(q_1+q_2)+l_1\ \cos(q_1)+l_{cm,3}\ \cos(q_1+q_2+q_3))+gm_2(l_{cm,2}\ \cos(q_1+q_2)+l_1\ \cos(q_1))$$

$$\mathbf{g}_2(\mathbf{q}_d) = 0$$

$$\mathbf{g}_3(\mathbf{q}_d) = g(m+m_1+m_2+m_3)$$

$$\mathbf{g}_4(\mathbf{q}_d) = gm_3(l_s\ \cos(q_1+q_2)+l_{cm,3}\ \cos(q_1+q_2+q_3))+gm_2l_{cm,2}\ \cos(q_1+q_2)$$

$$\mathbf{g}_5(\mathbf{q}_d) = gl_{cm,3}m_3\ \cos(q_1+q_2+q_3)$$

$$\mathbf{g}_6(\mathbf{q}_d) = gm_5(l_{cm,5}\ \cos(q_4+q_5)+l_4\ \cos(q_4))+gl_{cm,4}m_4\cos(q_4)$$

$$\mathbf{g}_7(\mathbf{q}_d) = gl_{cm,5}m_5\ \cos(q_4+q_3)$$

Vector $\boldsymbol{\phi}$ terms are listed as follows:

$$\boldsymbol{\phi}_1(\mathbf{q}_d) = l_2\ \cos(q_1+q_2)+l_1\ \cos(q_1)-l_f\ \cos(q_4)-l_c\ \ \cos(\theta)$$

$$\boldsymbol{\phi}_2(\mathbf{q}_d) = l_2\ \sin(q_1+q_2)+l_1\ \sin(q_1)-l_f\ \sin(q_4)-l_c\ \sin(\theta)$$

$$\boldsymbol{\phi}_3(\mathbf{q}_d) = l_s\ \cos(q_1+q_2)-l_t\ \cos(q_4+q_5)+l_1\ \cos(q_1)-l_4\ \cos(q_4)-l_c\ \cos(\theta)+l_3\ \cos(q_1+q_2+q_3)$$

$$\boldsymbol{\phi}_4(\mathbf{q}_d) = l_s\ \sin(q_1+q_2)-l_t\ \sin(q_4+q_5)+l_1\ \sin(q_1)-l_4\ \sin(q_4)-l_c\ \sin(\theta)+l_3\ \sin(q_1+q_2+q_3)$$

Appendix B

The singularly perturbed dynamics are given in Eq. (B1). However, the analytical solution for $\mathbf{H}(\mathbf{q}, \mathbf{z})$, $\mathbf{C}(\mathbf{q}, \dot{\mathbf{q}}, \mathbf{z}, \dot{\mathbf{z}})$, and $\mathbf{g}(\mathbf{q}, \mathbf{z})$ is non-existent. We have to suffice with the numerical solution. Here, we show the steps to numerically calculate the corresponding matrices

$$\begin{bmatrix} \mathbf{H}(\mathbf{q}, \mathbf{z}) & \mathbf{0}_{3\times4} \\ \mathbf{0}_{4\times3} & \mathbf{J}_z(\mathbf{q}, \mathbf{z}) \end{bmatrix} \begin{bmatrix} \ddot{\mathbf{q}} \\ \dot{\mathbf{z}} \end{bmatrix} = \begin{bmatrix} -\mathbf{C}(\mathbf{q}, \dot{\mathbf{q}}, \mathbf{z}, \dot{\mathbf{z}})\dot{\mathbf{q}} - \mathbf{g}(\mathbf{q}, \mathbf{z}) + \mathbf{B}\boldsymbol{\tau} \\ -\frac{1}{\varepsilon}\boldsymbol{\phi}(\mathbf{q}, \mathbf{z}) - \mathbf{J}_q(\mathbf{q}, \mathbf{z})\dot{\mathbf{q}} \end{bmatrix} \tag{B1}$$

The first bundle of equations in Eq. (14) are arrived at by the following steps. All unlisted terms are zero

$$\boldsymbol{\Gamma}_{1,1}(\mathbf{q}, \mathbf{z}) = -l_2 \sin(q_1 + q_2) - l_1 \sin(q_1)$$

$$\boldsymbol{\Gamma}_{1,4}(\mathbf{q}, \mathbf{z}) = -l_2 \sin(q_1 + q_2)$$

$$\boldsymbol{\Gamma}_{1,6}(\mathbf{q}, \mathbf{z}) = l_f \sin(q_4)$$

$$\boldsymbol{\Gamma}_{2,1}(\mathbf{q}, \mathbf{z}) = l_2 \cos(q_1 + q_2) + l_1 \cos(q_1)$$

$$\boldsymbol{\Gamma}_{2,4}(\mathbf{q}, \mathbf{z}) = l_2 \cos(q_1 + q_2)$$

$$\boldsymbol{\Gamma}_{2,6}(\mathbf{q}, \mathbf{z}) = -l_f \cos(q_4)$$

$$\boldsymbol{\Gamma}_{3,1}(\mathbf{q}, \mathbf{z}) = -l_s \sin(q_1 + q_2) - l_1 \sin(q_1) - l_3 \sin(q_1 + q_2 + q_3)$$

$$\boldsymbol{\Gamma}_{3,4}(\mathbf{q}, \mathbf{z}) = -l_s \sin(q_1 + q_2) - l_3 \sin(q_1 + q_2 + q_3)$$

$$\boldsymbol{\Gamma}_{3,5}(\mathbf{q}, \mathbf{z}) = -l_3 \sin(q_1 + q_2 + q_3)$$

$$\boldsymbol{\Gamma}_{3,6}(\mathbf{q}, \mathbf{z}) = l_t \sin(q_4 + q_5) + l_4 \sin(q_4)$$

$$\boldsymbol{\Gamma}_{3,7}(\mathbf{q}, \mathbf{z}) = l_t \sin(q_4 + q_5)$$

$$\boldsymbol{\Gamma}_{4,1}(\mathbf{q}, \mathbf{z}) = l_s \cos(q_1 + q_2) + l_1 \cos(q_1) + l_3 \cos(q_1 + q_2 + q_3)$$

$$\boldsymbol{\Gamma}_{4,4}(\mathbf{q}, \mathbf{z}) = l_s \cos(q_1 + q_2) + l_3 \cos(q_1 + q_2 + q_3)$$

$$\boldsymbol{\Gamma}_{4,5}(\mathbf{q}, \mathbf{z}) = l_3 \cos(q_1 + q_2 + q_3)$$

$$\boldsymbol{\Gamma}_{4,6}(\mathbf{q}, \mathbf{z}) = -l_t \cos(q_4 + q_5) - l_4 \cos(q_4)$$

$$\boldsymbol{\Gamma}_{4,7}(\mathbf{q}, \mathbf{z}) = -l_t \cos(q_4 + q_5)$$

$$\boldsymbol{\Gamma}_{5,1}(\mathbf{q}, \mathbf{z}) = \Gamma_{6,2}(q, z) = \Gamma_{7,3}(q, z) = 1$$

$$\boldsymbol{\Gamma}_{1,1}(\dot{\mathbf{q}}, \dot{\mathbf{z}}) = -\dot{q}_1 l_1 \cos(q_1) - l_2 \cos(q_1 + q_2)(\dot{q}_1 + \dot{q}_2)$$

$$\boldsymbol{\Gamma}_{1,4}(\dot{\mathbf{q}}, \dot{\mathbf{z}}) = -l_2 \cos(q_1 + q_2)\,(\dot{q}_1 + \dot{q}_2)$$

$$\boldsymbol{\Gamma}_{1,6}(\dot{\mathbf{q}}, \dot{\mathbf{z}}) = \dot{q}_4 l_f \cos(q_4)$$

$$\boldsymbol{\Gamma}_{2,1}(\dot{\mathbf{q}}, \dot{\mathbf{z}}) = -\dot{q}_1 l_1 \sin(q_1) - l_2 \sin(q_1 + q_2)(\dot{q}_1 + \dot{q}_2)$$

$$\boldsymbol{\Gamma}_{2,4}(\dot{\mathbf{q}}, \dot{\mathbf{z}}) = -l_2 \sin(q_1 + q_2)(\dot{q}_1 + \dot{q}_2)$$

$$\boldsymbol{\Gamma}_{2,6}(\dot{\mathbf{q}}, \dot{\mathbf{z}}) = \dot{q}_4 l_f \sin(q_4)$$

$$\boldsymbol{\Gamma}_{3,1}(\dot{\mathbf{q}}, \dot{\mathbf{z}}) = -\dot{q}_1 l_1 \cos(q_1) - l_3 \cos(q_1 + q_2 + q_3)(\dot{q}_1 + \dot{q}_2 + \dot{q}_3) - l_s \cos(q_1 + q_2)(\dot{q}_1 + \dot{q}_2)$$

$$\boldsymbol{\Gamma}_{3,4}(\dot{\mathbf{q}}, \dot{\mathbf{z}}) = -l_3 \cos(q_1 + q_2 + q_3)(\dot{q}_1 + \dot{q}_2 + \dot{q}_3) - l_s \cos(q_1 + q_2)(\dot{q}_1 + \dot{q}_2)$$

$$\boldsymbol{\Gamma}_{3,5}(\dot{\mathbf{q}}, \dot{\mathbf{z}}) = -l_3 \cos(q_1 + q_2 + q_3)(\dot{q}_1 + \dot{q}_2 + \dot{q}_3)$$

$$\mathbf{\Gamma}_{3,6}(\dot{\mathbf{q}}, \dot{\mathbf{z}}) = \dot{q}_4 l_4 \cos(q_4) + l_t \cos(q_4 + q_5)(\dot{q}_4 + \dot{q}_5)$$

$$\mathbf{\Gamma}_{3,7}(\dot{\mathbf{q}}, \dot{\mathbf{z}}) = l_t \cos(q_4 + q_5)(\dot{q}_4 + \dot{q}_5)$$

$$\mathbf{\Gamma}_{4,1}(\dot{\mathbf{q}}, \dot{\mathbf{z}}) = \dot{q}_1 l_1 \sin(q_1) - l_3 \sin(q_1 + q_2 + q_3)(\dot{q}_1 + \dot{q}_2 + \dot{q}_3) - l_s \cos(q_1 + q_2)(\dot{q}_1 + \dot{q}_2)$$

$$\mathbf{\Gamma}_{4,4}(\dot{\mathbf{q}}, \dot{\mathbf{z}}) = -l_3 \sin(q_1 + q_2 + q_3)(\dot{q}_1 + \dot{q}_2 + \dot{q}_3) - l_s \cos(q_1 + q_2)(\dot{q}_1 + \dot{q}_2)$$

$$\mathbf{\Gamma}_{4,5}(\dot{\mathbf{q}}, \dot{\mathbf{z}}) = -l_3 \sin(q_1 + q_2 + q_3)(\dot{q}_1 + \dot{q}_2 + \dot{q}_3)$$

$$\mathbf{\Gamma}_{4,6}(\dot{\mathbf{q}}, \dot{\mathbf{z}}) = \dot{q}_4 l_4 \sin(q_4) + l_t \sin(q_4 + q_5)(\dot{q}_4 + \dot{q}_5)$$

$$\mathbf{\Gamma}_{4,7}(\dot{\mathbf{q}}, \dot{\mathbf{z}}) = l_t \sin(q_4 + q_5)(\dot{q}_4 + \dot{q}_5)$$

Finally, the second bundle of equations results in

$$\mathbf{J}_{q(1,1)}(\mathbf{q}, \mathbf{z}) = -l_2 \sin(q_1 + q_2) - l_1 \sin(q_1)$$

$$\mathbf{J}_{q(2,1)}(\mathbf{q}, \mathbf{z}) = l_2 \cos(q_1 + q_2) + l_1 \cos(q_1)$$

$$\mathbf{J}_{q(3,1)}(\mathbf{q}, \mathbf{z}) = -l_s \sin(q_1 + q_2) - l_1 \sin(q_1) - l_3 \sin(q_1 + q_2 + q_3)$$

$$\mathbf{J}_{q(4,1)}(\mathbf{q}, \mathbf{z}) = l_s \cos(q_1 + q_2) + l_1 \cos(q_1) + l_3 \cos(q_1 + q_2 + q_3)$$

$$\mathbf{J}_{z(1,1)}(\mathbf{q}, \mathbf{z}) = -l_2 \sin(q_1 + q_2)$$

$$\mathbf{J}_{z(1,3)}(\mathbf{q}, \mathbf{z}) = l_f \sin(q_4)$$

$$\mathbf{J}_{z(2,1)}(\mathbf{q}, \mathbf{z}) = l_2 \cos(q_1 + q_2)$$

$$\mathbf{J}_{z(2,3)}(\mathbf{q}, \mathbf{z}) = -l_f \cos(q_4)$$

$$\mathbf{J}_{z(3,1)}(\mathbf{q}, \mathbf{z}) = -l_s \sin(q_1 + q_2) - l_3 \sin(q_1 + q_2 + q_3)$$

$$\mathbf{J}_{z(3,2)}(\mathbf{q}, \mathbf{z}) = -l_3 \sin(q_1 + q_2 + q_3)$$

$$\mathbf{J}_{z(3,3)}(\mathbf{q}, \mathbf{z}) = l_t \sin(q_4 + q_5) + l_4 \sin(q_4)$$

$$\mathbf{J}_{z(3,4)}(\mathbf{q}, \mathbf{z}) = l_t \sin(q_4 + q_5)$$

$$\mathbf{J}_{z(4,1)}(\mathbf{q}, \mathbf{z}) = l_s \cos(q_1 + q_2) + l_3 \cos(q_1 + q_2 + q_3)$$

$$\mathbf{J}_{z(4,2)}(\mathbf{q}, \mathbf{z}) = l_3 \cos(q_1 + q_2 + q_3)$$

$$\mathbf{J}_{z(4,3)}(\mathbf{q}, \mathbf{z}) = -l_t \cos(q_4 + q_5) - l_4 \cos(q_4)$$

$$\mathbf{J}_{z(4,4)}(\mathbf{q}, \mathbf{z}) = -l_t \cos(q_4 + q_5)$$

The same process applies for arriving at the SPF stance-phase dynamics.

References

[1] Ananthanarayanan, A., Azadi, M., and Kim, S., 2012, "Towards a Bio-Inspired Leg Design for High-Speed Running," Bioinspir. Biomim., **7**(4), p. 046005.

[2] Hutter, M., Gehring, C., Jud, D., Lauber, A., Bellicoso, C. D., Tsounis, V., Hwangbo, J., Bodie, K., Fankhauser, P., Bloesch, M., and Diethelm, R., 2016, "Anymal—A Highly Mobile and Dynamic Quadrupedal Robot," IEEE/RSJ International Conference on Intelligent Robots and Systems, Daejeon, South Korea, Oct. 9–14, pp. 38–44.

[3] Semini, C., Tsagarakis, N. G., Guglielmino, E., Focchi, M., Cannella, F., and Caldwell, D. G., 2011, "Design of HyQ—A Hydraulically and Electrically Actuated Quadruped Robot," Proc. Inst. Mech. Eng. Part I: J. Syst. Control Eng., **225**(6), pp. 831–849.

[4] Seok, S., Wang, A., Chuah, M. Y., Otten, D., Lang, J., and Kim, S., 2013, "Design Principles for Highly Efficient Quadrupeds and Implementation on the MIT Cheetah Robot," IEEE International Conference on Robotics and Automation, Karlsruhe, Germany, May 6–10, pp. 3307–3312.

[5] Todd, D. J., 2013, *Walking Machines: An Introduction to Legged Robots*, Springer, Berlin.

[6] Alamdari, A., and Krovi, V. N., 2016, "Design of Articulated Leg–Wheel Subsystem by Kinetostatic Optimization," Mech. Mach. Theory, **100**, pp. 222–234.

[7] Alamdari, A., and Krovi, V., 2016, "Design and Analysis of a Cable-Driven Articulated Rehabilitation System for Gait Training," ASME J. Mech. Robot., **8**(5), p. 051018.
[8] Alamdari, A., and Krovi, V. N., 2016, "Static Balancing of Highly Reconfigurable Articulated Wheeled Vehicles for Power Consumption Reduction of Actuators," Int. J. Mech. Rob. Syst., **3**(1), pp. 15–31.
[9] Alamdari, A., Haghighi, R., and Krovi, V., 2018, "Stiffness Modulation in an Elastic Articulated-Cable Leg-Orthosis Emulator: Theory and Experiment," IEEE Trans. Robot., **34**(5), pp. 1266–1279.
[10] Alamdari, A., Haghighi, R., and Krovi, V., 2019, "Gravity-Balancing of Elastic Articulated-Cable Leg-Orthosis Emulator," Mech. Mach. Theory, **131**, pp. 351–370.
[11] Saab, W., Rone, W. S., Kumar, A., and Ben-Tzvi, P., 2019, "Design and Integration of a Novel Spatial Articulated Robotic Tail," IEEE/ASME Trans. Mechatron., **24**(2), pp. 434–446.
[12] Rone, W. S., Saab, W., and Ben-Tzvi, P., 2018, "Design, Modeling, and Integration of a Flexible Universal Spatial Robotic Tail," ASME J. Mech. Robot., **10**(4), p. 041001.
[13] Liu, Y., Wang, J., and Ben-Tzvi, P., 2019, "A Cable Length Invariant Robotic Tail Using a Circular Shape Universal Joint Mechanism," ASME J. Mech. Robot., **11**(5), p. 051005.
[14] Rone, W. S., Saab, W., Kumar, A., and Ben-Tzvi, P., 2019, "Controller Design, Analysis, and Experimental Validation of a Robotic Serpentine Tail to Maneuver and Stabilize a Quadrupedal Robot," J. Dyn. Syst. Meas. Control, **141**(8), p. 081002.
[15] Rone, W. S., Liu, Y., and Ben-Tzvi, P., 2019, "Maneuvering and Stabilization Control of a Bipedal Robot With a Universal-Spatial Robotic Tail," Bioinspir. Biomim., **14**(1), p. 016014.
[16] Patel, A., and Boje, E., 2015, "On the Conical Motion of a Two-Degree-of-Freedom Tail Inspired by the Cheetah," IEEE Trans. Robot., **31**(6), pp. 1555–1560.
[17] De, A., and Koditschek, D. E., 2015, "Parallel Composition of Templates for Tail-Energized Planar Hopping," IEEE International Conference on Robotics and Automation, Seattle, WA, May 26–30, pp. 4562–4569.
[18] Casarez, C. S., and Fearing, R. S., 2018, "Steering of an Underactuated Legged Robot Through Terrain Contact With an Active Tail," IEEE/RSJ International Conference on Intelligent Robots and Systems, Madrid, Spain, Oct. 1–5, pp. 2739–2746.
[19] Heim, S. W., Ajallooeian, M., Eckert, P., Vespignani, M., and Ijspeert, A. J., 2016, "On Designing an Active Tail for Legged Robots: Simplifying Control via Decoupling of Control Objectives," Ind. Robot, **43**(3), pp. 338–346.
[20] Tavolieri, C., Ottaviano, E., Ceccarelli, M., and Rienzo, A. D., 2006, "Analysis and Design of a 1-DOF Leg for Walking Machines," 15th International Workshop on Robotics in Alpe-Adria-Danube Region (RAAD), Balatonfured, Hungary, June, 2006, pp. 15–17.
[21] Ghassaei, A., 2011, "The Design and Optimization of a Crank-Based Leg Mechanism," Ph.D. thesis, Pomona College, Pomona, CA.
[22] Park, J., Kim, K.-S., and Kim, S., 2014, "Design of a Cat-Inspired Robotic Leg for Fast Running," Adv. Robot., **28**(23), pp. 1587–1598.
[23] Kamidi, V. R., Saab, W., and Ben-Tzvi, P., 2017, "Design and Analysis of a Novel Planar Robotic Leg for High-Speed Locomotion," IEEE/RSJ International Conference on Intelligent Robots and Systems, Vancouver, Canada, Sept. 24–28, pp. 6343–6348.
[24] Seyfarth, A., Geyer, H., and Herr, H., 2003, "Swing-leg Retraction: a Simple Control Model for Stable Running," J. Exp. Biol., **206**(15), pp. 2547–2555.
[25] Poulakakis, I., Smith, J. A., and Buehler, M., 2005, "Modeling and Experiments of Untethered Quadrupedal Running With a Bounding Gait: The Scout II Robot," Int. J. Robot. Res., **24**(4), pp. 239–256.
[26] Brenan, K., Campbell, S., and Petzold, L., 1995, *Numerical Solution of Initial-Value Problems in Differential-Algebraic Equations, Society for Industrial and Applied Mathematics*, Philadelphia.
[27] Petzold, L. R., 1992, "Numerical Solution of Differential-Algebraic Equations in Mechanical Systems Simulation," Phys. D, **60**(1–4), pp. 269–279.
[28] Krishnan, H., and McClamroch, N. H., 1994, "Tracking in Nonlinear Differential-Algebraic Control Systems With Applications to Constrained Robot Systems," Automatica, **30**(12), pp. 1885–1897.
[29] Ghorbel, F., Chételat, O., and Longchamp, R., 1994, "A Reduced Model for Constrained Rigid Bodies With Application to Parallel Robots," IFAC Proc. Vol., **27**(14), pp. 57–62.
[30] Gear, C. W., Leimkuhler, B., and Gupta, G. K., 1985, "Automatic Integration of Euler-Lagrange Equations With Constraints," J. Comput. Appl. Math., **12**, pp. 77–90.
[31] Baumgarte, J., 1972, "Stabilization of Constraints and Integrals of Motion in Dynamical Systems," Computer Methods Appl. Mech. Eng., **1**(1), pp. 1–16.
[32] Ascher, U. M., Chin, H., Petzold, L. R., and Reich, S., 1995, "Stabilization of Constrained Mechanical Systems With DAEs and Invariant Manifolds," J. Struct. Mech., **23**(2), pp. 135–157.
[33] Wang, Z., and Ghorbel, F. H., 2006, "Control of Closed Kinematic Chains: A Comparative Study," American Control Conference, Minneapolis, MN, June 14–16, pp. 2498–2503.
[34] Yun, X., and Sarkar, N., 1998, "Unified Formulation of Robotic Systems With Holonomic and Nonholonomic Constraints," IEEE Trans. Rob. Autom., **14**(4), pp. 640–650.
[35] Ghorbel, F. H., Chételat, O., Gunawardana, R., and Longchamp, R., 2000, "Modeling and Set Point Control of Closed-Chain Mechanisms: Theory and Experiment," IEEE Trans. Control Syst. Technol., **8**(5), pp. 801–815.
[36] Gordon, B. W., and Liu, S., 1998, "A Singular Perturbation Approach for Modeling Differential-Algebraic Systems," J. Dyn. Syst. Meas. Control, **120**(4), pp. 541–545.
[37] Dabney, J. B., Ghorbel, F. H., and Wang, Z., 2002, "Modeling Closed Kinematic Chains via Singular Perturbations," American Control Conference, Anchorage, AK, May 8–10, pp. 4104–4110.
[38] Wang, Z., Ghorbel, F. H., and Dabney, J. B., 2004, "On the Domain and Error Characterization in the Singular Perturbation Modeling of Closed Kinematic Chains," American Control Conference, Boston, MA, June 30–July 2, pp. 493–498.
[39] Wang, Z., and Ghorbel, F. H., 2006, "Control of Closed Kinematic Chains Using a Singularly Perturbed Dynamics Model," J. Dyn. Syst. Meas. Control, **128**(1), pp. 142–151.
[40] Hyun, D. J., Lee, J., Park, S., and Kim, S., 2016, "Implementation of Trot-to-Gallop Transition and Subsequent Gallop on the MIT Cheetah I," Int. J. Robot. Res., **35**(13), pp. 1627–1650.
[41] Hutter, M., Remy, C. D., Höpflinger, M. A., and Siegwart, R., 2010, "Slip Running With an Articulated Robotic Leg," IEEE/RSJ International Conference on Intelligent Robots and Systems, Taipei, Taiwan, Oct. 18–22, pp. 4934–4939.
[42] Westervelt, E. R., Grizzle, J. W., Chevallereau, C., Choi, J. H., and Morris, B., 2018, *Feedback Control of Dynamic Bipedal Robot Locomotion*, CRC Press, Boca Raton, FL.
[43] Grizzle, J. W., Chevallereau, C., Sinnet, R. W., and Ames, A. D., 2014, "Models, Feedback Control, and Open Problems of 3D Bipedal Robotic Walking," Automatica, **50**(8), pp. 1955–1988.
[44] Wittenburg, J., 2007, *Dynamics of Multibody Systems*, Springer, Berlin.
[45] Hurmuzlu, Y., and Marghitu, D. B., 1994, "Rigid Body Collisions of Planar Kinematic Chains With Multiple Contact Points," Int. J. Rob. Res., **13**(1), pp. 82–92.
[46] Kumar, A., and Ben-Tzvi, P., 2016, "Spatial Object Tracking System Based on Linear Optical Sensor Arrays," IEEE Sens. J., **16**(22), pp. 7933–7940.